Biogeosciences Discuss., 11, 5711–5742, 2014
www.biogeosciences-discuss.net/11/5711/2014/
doi:10.5194/bgd-11-5711-2014

Biogeosciences Discussions Open Access

Local spatial structure of forest biomass and its consequences for remote sensing of carbon stocks

M. Réjou-Méchain[1], H. C. Muller-Landau[2], M. Detto[2], S. C. Thomas[3], T. Le Toan[4], S. S. Saatchi[5], J. S. Barreto-Silva[6], N. A. Bourg[7], S. Bunyavejchewin[8], N. Butt[9,10], W. Y. Brockelman[11], M. Cao[12], D. Cárdenas[13], J.-M. Chiang[14], G. B. Chuyong[15], K. Clay[16], R. Condit[2], H. S. Dattaraja[17], S. J. Davies[18], A. Duque[19], S. Esufali[20], C. Ewango[21], R. H. S. Fernando[22], C. D. Fletcher[23], I. A. U. N. Gunatilleke[20], Z. Hao[24], K. E. Harms[25], T. B. Hart[26], B. Hérault[27], R. W. Howe[28], S. P. Hubbell[2,29], D. J. Johnson[16], D. Kenfack[30], A. J. Larson[31], L. Lin[12], Y. Lin[14], J. A. Lutz[32], J.-R. Makana[33], Y. Malhi[9], T. R. Marthews[9], R. W. McEwan[34], S. M. McMahon[35], W. J. McShea[7], R. Muscarella[36], A. Nathalang[11], N. S. M. Noor[23], C. J. Nytch[37], A. A. Oliveira[38], R. P. Phillips[16], N. Pongpattananurak[39], R. Punchi-Manage[40], R. Salim[23], J. Schurman[3], R. Sukumar[17], H. S. Suresh[17], U. Suwanvecho[11], D. W. Thomas[41], J. Thompson[36,42], M. Uríarte[36], R. Valencia[43], A. Vicentini[44], A. T. Wolf[28], S. Yap[45], Z. Yuan[24], C. E. Zartman[44], J. K. Zimmerman[37], and J. Chave[1]

[1]Laboratoire Evolution et Diversité Biologique, UMR 5174 CNRS, Université Paul Sabatier, 31062 Toulouse, France
[2]Smithsonian Tropical Resource Institute, Apartado Postal 0843-03092 Balboa, Ancon, Panama
[3]University of Toronto, Faculty of Forestry, Toronto, Canada
[4]Centre d'Etudes Spatiales de la Biosphère, UMR 5126 CNRS, CNES, Université Paul Sabatier, IRD, 31401 Toulouse, France
[5]Jet Propulsion Laboratory, California Institute of Technology, Pasadena, CA 91109, USA
[6]Instituto Amazónico de Investigaciones Científicas SINCHI, Avenida Vásquez Cobo entre calles 15 y 16, Leticia, Amazonas, Colombia
[7]Conservation Ecology Center Smithsonian Conservation Biology Institute National Zoological Park 1500 Remount Rd., Front Royal, VA 22630, USA
[8]National Parks, Wildlife and Plant Conservation Department, Research Office, Chatuchak, Bangkok 10900, Thailand
[9]Environmental Change Institute, School of Geography and the Environment, University of Oxford, Oxford OX1 3QY, UK
[10]ARC Centre of Excellence for Environmental Decisions, School of Biological Sciences, The University of Queensland, St. Lucia, 4072, Australia
[11]Ecology Lab, Bioresources Technology Unit, 113 Science Park, Paholyothin Road, Khlong 1, Khlongluang, Pathum Thani 12120, Thailand
[12]Key Laboratory of Tropical Forest Ecology, Xishuangbanna Tropical Botanical Garden, Chinese Academy of Sciences, Kunming 650223, China
[13]Instituto Amazónico de Investigaciones Científicas SINCHI. Calle 20 No. 5–44. Bogotá Colombia
[14]Department of Life Science, Tunghai University, Taichung 40704, Taiwan
[15]Department of Plant and Animal Sciences, University of Buea, P.O. Box 63, Buea, Cameroon
[16]Department of Biology, Indiana University, Jordan Hall, 1001 East Third Street, Bloomington, IN 47405, USA
[17]Center for Ecological Sciences, Indian Institute of Science, Bangalore 560012, India
[18]Center for Tropical Forest Science, Smithsonian Institution Global Earth Observatory, Smithsonian Tropical Research Institute, P.O. Box 37012, Washington, DC 20012, USA

BGD
11, 5711–5742, 2014

[19]Departamento de Ciencias Forestales, Universidad Nacional de Colombia, Sede Medellín, Calle 59A No 63-20, Medellín, Colombia
[20]Department of Botany, Faculty of Science, University of Peradeniya, Peradeniya, Sri Lanka
[21]Centre de Formation et de Recherche en Conservation Forestière (CEFRECOF), Wildlife Conservation Society, Kinshasa, DR Congo
[22]Royal Botanical Garden, Peradeniya, Sri Lanka
[23]Forest Research Institute Malaysia (FRIM), 52109 Kepong, Selangor, Malaysia
[24]State Key Laboratory of Forest and Soil Ecology, Institute of Applied Ecology, Chinese Academy of Sciences, Shenyang 110164, China
[25]Department of Biological Sciences, Louisiana State University, Baton Rouge, LA 70803, USA
[26]Project TL2, Kinshasa, DR Congo
[27]Cirad, UMR Ecologie des Forêts de Guyane (EcoFoG), Campus Agronomique, BP701, 97310 Kourou, French Guiana
[28]Department of Natural and Applied Sciences, University of Wisconsin-Green Bay, Green Bay, WI 54311, USA
[29]Department of Ecology and Evolutionary Biology, University of California, Los Angeles, CA 90095, USA
[30]CTFS-Arnold Arboretum Office, Harvard University, 22 Divinity Avenue, Cambridge, MA 02138, USA
[31]Department of Forest Management, College of Forestry and Conservation, The University of Montana, Missoula, MT 59812, USA
[32]Wildland Resources Department, Utah State University, 5230 Old Main Hill, Logan, UT 84322-5230, USA
[33]Wildlife Conservation Society – DRC Program, Kinshasa, DR Congo
[34]Department of Biology, University of Dayton, Dayton, OH 45469-2320, USA
[35]Smithsonian Tropical Research Institute & Smithsonian Environmental Research Center, Edgewater, Maryland, USA
[36]Department of Ecology, Evolution & Environmental Biology, Columbia University, New York, NY, USA
[37]Department of Environmental Science, University of Puerto Rico, Box 70377, Rio Piedras, San Juan, 00936-8377, Puerto Rico

BGD
11, 5711–5742, 2014

[38]Departamento de Ecologia, Instituto de Biociências, Universidade de São Paulo, 04582050 São Paulo, Brazil
[39]Department of Conservation, Faculty of Forestry, Kasetsart University, Bangkok, Thailand
[40]Department of Ecosystem Modelling, University of Göttingen, Göttingen, Germany
[41]Department of Botany and Plant Pathology, Oregon State University, Corvallis, OR 97331, USA
[42]Centre for Ecology & Hydrology, Edinburgh, Bush Estate, Penicuik, Midlothian, Scotland EH26 0QB, UK
[43]Escuela de Ciencias Biológicas, Pontificia Universidad Católica del Ecuador, Apartado 17-01-2184, Quito, Ecuador
[44]Instituto Nacional de Pesquisas da Amazônia, Manaus, AM, Brazil
[45]Institute of Biology University of the Philippines Diliman, Quezon City 1101, Philippines

Received: 31 March 2014 – Accepted: 3 April 2014 – Published: 22 April 2014

Correspondence to: M. Réjou-Méchain (maxime.rejou@gmail.com)

Published by Copernicus Publications on behalf of the European Geosciences Union.

Abstract

Advances in forest carbon mapping have the potential to greatly reduce uncertainties in the global carbon budget and to facilitate effective emissions mitigation strategies such as REDD+. Though broad scale mapping is based primarily on remote sensing data, the accuracy of resulting forest carbon stock estimates depends critically on the quality of field measurements and calibration procedures. The mismatch in spatial scales between field inventory plots and larger pixels of current and planned remote sensing products for forest biomass mapping is of particular concern, as it has the potential to introduce errors, especially if forest biomass shows strong local spatial variation. Here, we used 30 large (8–50 ha) globally distributed permanent forest plots to quantify the spatial variability in aboveground biomass (AGB) at spatial grains ranging from 5 to 250 m (0.025–6.25 ha), and we evaluate the implications of this variability for calibrating remote sensing products using simulated remote sensing footprints. We found that the spatial sampling error in AGB is large for standard plot sizes, averaging 46.3 % for 0.1 ha subplots and 16.6 % for 1 ha subplots. Topographically heterogeneous sites showed positive spatial autocorrelation in AGB at scales of 100 m and above; at smaller scales, most study sites showed negative or nonexistent spatial autocorrelation in AGB. We further show that when field calibration plots are smaller than the remote sensing pixels, the high local spatial variability in AGB leads to a substantial "dilution" bias in calibration parameters, a bias that cannot be removed with current statistical methods. Overall, our results suggest that topography should be explicitly accounted for in future sampling strategies and that much care must be taken in designing calibration schemes if remote sensing of forest carbon is to achieve its promise.

BGD
11, 5711–5742, 2014

1 Introduction

Forests represent the largest aboveground carbon stock in the terrestrial biosphere, and forest degradation and regrowth are globally important carbon fluxes (Pan et al., 2011). However, our ability to predict future atmospheric CO_2 concentrations or to implement effective carbon emission mitigation strategies (e.g. REDD+; Miles and Kapos, 2008) is limited by the accuracy of forest carbon stock estimates. The global monitoring of forest carbon stocks has thus come to the fore of the research agenda, with important implications in economics, policy and conservation (Gibbs et al., 2007). In recent years, aboveground carbon stock estimates based on field inventories and on remote sensing approaches have led to substantial progress in mapping broad-scale carbon stocks (Asner et al., 2010; Baccini et al., 2012; Malhi et al., 2006; Saatchi et al., 2011). However, substantial uncertainties are still associated with such carbon maps (Mitchard et al., 2013b).

Given the prohibitive cost of field and/or airborne campaigns to survey vegetation at broad spatial scales, space-based sensing of vegetation will probably soon dominate efforts to map and monitor forest carbon stocks beyond the landscape scale (Goetz and Dubayah, 2011; Wulder et al., 2012). Active remote sensing tools such as Light Detection and Ranging (LiDAR) and/or synthetic aperture radar (SAR) are currently the best candidates for forest carbon mapping at broad spatial scales. Two forthcoming spaceborne missions are thus of particularly interest: the LiDAR-based ICESAT2 mission (scheduled for launch in late 2015; Abdalati et al., 2010) and the P-band radar BIOMASS mission (scheduled for launch in 2020; Le Toan et al., 2011). Both instruments will have a relatively coarse resolution (50 m for ICESAT2 and 100–200 m for BIOMASS) and will rely on field data to calibrate their inversion models. Hence, the quality of the resulting forest carbon map will depend crucially on the accuracy and suitability of the field data used for calibration.

The quality of a field-based calibration and resulting products depends fundamentally on the degree to which forest biomass in entire pixels is represented by the field

BGD
11, 5711–5742, 2014

data. In space-based remote sensing of forest biomass, sensor footprints are usually several to many times larger than field calibration plots (Baccini et al., 2007). If forest biomass is homogenous within pixel-sized areas, this mismatch in sample area will have little impact on calibration; however, if there is substantial local heterogeneity in biomass, then small ground samples will have large sampling errors. In general, the uncertainty associated with any field biomass estimate decreases as the sampling area increases. If sampling uncertainty is large, it is likely that the biomass maps calibrated using such field-based data will be unreliable. Furthermore, the remote sensing field of view is often different from the field-based one for several reasons including geolocalisation errors, the post-geoprocessing conversion of the ellipsoidal footprint into a square pixel, and the difference between the forest components measured (e.g. remote sensing canopy structure vs. field-based tree stem measurements; Mascaro et al., 2011). Such spatial mismatches may considerably increase the errors during the calibration step. There is thus a need to quantify these errors and test potential strategies to address them.

From a global perspective, ground sampling of forests is unevenly distributed. Over a million of forest inventory plots have been established across the temperate zone, with a high diversity in plot designs. For example, hundreds of thousands of permanent plots of approximately 0.1 ha are being monitored throughout the USA and Sweden (Bechtold and Patterson, 2005; Ranneby et al., 1987). However, in spite of the United Nations Food and Agricultural Organization Forestry programs, many areas, especially in the tropics, lack forest inventories. Individual scientists, sometimes working in collaborative networks, have collected data in hundreds of large plots (≥ 1 ha) in the tropics (Condit, 1995; Lewis et al., 2009; Phillips et al., 2009). Though these collections of field plots do not represent systematic or random samples, they are routinely used to estimate forest carbon storage or to calibrate remote sensing models (Asner et al., 2013; Baccini et al., 2012; Chave et al., 2008; Malhi et al., 2006; Saatchi et al., 2011). Yet, little attention has been given to quantifying the error associated with the field sampling strategies, or to propagating this error to remote sensing estimates of carbon stocks

BGD
11, 5711–5742, 2014

(but for notable exceptions see Gonzalez et al., 2010; Mermoz et al., 2014). This is the focus of the present study.

Here, we applied spatial statistic methods to forest stand level census data from a global network of 30 large permanent plots (8 to 50 ha) established in natural forests (Condit, 1998; Losos and Leigh, 2004) to simulate the range of ground forest sampling strategies and explore related uncertainties (Fig. 1; Supplement, Table S1). Using these very large plots, we address three main questions: (1) how large are field-sampling errors in aboveground biomass (AGB) stock, how do they vary across sites, forest types, and continents, and how do they scale with the area sampled? (2) What is the local spatial structure of AGB, and how does this spatial structure vary among sites? (3) What are the implications of field sampling error for the accuracy of remote sensing calibration equations under different calibration plot and remote sensing footprint areas, and different bias-correction procedures?

2 Material and methods

2.1 Field data

We used standardized measurements in 30 large forest plots across three continents (8–50 ha each, Fig. 1 and Table S1). In 28 of the plots, all free-standing trees ≥ 1 cm dbh (diameter measured to the nearest millimeter at 130 cm above the ground or 50 cm above buttresses) were mapped, tagged, and identified taxonomically (Condit, 1998). In two additional plots, only trees ≥ 10 cm in dbh were included (Table S1). Trees < 10 cm dbh generally contribute less than 5 % of the total AGB in mature tropical forests (Chave et al., 2003). Aboveground biomass of each individual stem was estimated using regression models based on the measured individual diameter and the wood specific gravity assigned to that species and site, or site-specific allometric equations (details in Table S1). We used only data on free-standing woody stems, and excluded

BGD
11, 5711–5742, 2014

lianas from our analyses. Lianas generally represent less than 5 % of the total biomass (e.g. Schnitzer et al., 2012).

The range in elevation across 19 forest plots showed a strong and significant correlation with topographic heterogeneity (Fig. S1). We therefore used the range in elevation, a metric available over all sites, as a proxy for topographic heterogeneity.

2.2 Sampling error in AGB

Each plot was gridded into subplots at spatial resolutions ranging from 5 to 250 m, to the extent feasible given the plot dimensions. Within each subplot, AGB ($Mg\,ha^{-1}$) was calculated by summing AGB estimates for all trees whose stems were located within the subplot. We quantified the sampling error in AGB for subplots of area s (in ha) using the coefficient of variation of AGB among subplots, calculated as

$$\mathrm{CV}(s) = 100 \times \frac{\sigma(s)}{\mu} \tag{1}$$

where μ is the mean AGB in the plot, $\sigma(s)$ is the standard deviation in AGB computed from subplots of area s, and CV(s) is the coefficient of variation for plot area s in percent. A higher CV value indicates a higher spatial heterogeneity of AGB, and therefore higher sampling error.

We focused on the CV at the 1 ha scale, denoted CV(1) in our examination of variation in sampling errors among sites. We evaluated whether CV(1) increased with AGB among sites, and whether it increased with topographic heterogeneity as quantified by the elevation range, in both cases using nonparametric Spearman rank correlations. We also tested whether CV(1) varied significantly among continents or forest types using nonparametric Kruskal–Wallis tests.

To study the spatial scaling of sampling error with plot area, we fitted power functions to the relationship between CV and subplot area. In the absence of spatial autocorrelation (i.e. given independence of each grid cell), the central limit theorem implies that $\sigma(s) \sim \frac{1}{\sqrt{s}}$, so the logarithm of CV(s) should decrease linearly with ln(s),

BGD
11, 5711–5742, 2014

and with a slope of $-1/2$. Under these conditions, the sampling error of AGB is thus $CV(s) = \frac{CV(1)}{\sqrt{s}}$, where CV(1) is the coefficient of variation of 1 ha subplots. If spatial autocorrelation is present, we expect that $\sigma(s) \sim \frac{1}{s^\gamma}$, where $\gamma \neq \frac{1}{2}$. Positive spatial autocorrelation should yield $\gamma < \frac{1}{2}$; negative spatial autocorrelation $\gamma > \frac{1}{2}$. To test for the significance of departure of γ from $\frac{1}{2}$, we computed 95 % confidence intervals of γ using $CI = \gamma \pm t(\alpha, df) \times S_b$ where t is the Student's t distribution, α the significance level (here 0.975), df the degrees of freedom (here $n-2$) and S_b the estimated standard error in the slope.

2.3 Spatial autocorrelation in AGB

To analyze the spatial autocorrelation of AGB within field plots, we used wavelet-kernel functions (Percival, 1995). The wavelet transform analyses the variance across spatial scales s by decomposing the signal into an orthonormal wavelet basis, in our case the isotropic Morlet wavelet (see details in Appendix S1, Supplement). A wavelet variance lower than one at a given spatial grain s indicates a negative spatial autocorrelation, i.e. neighboring subplots with an area of s^2 are more different than expected under randomness, while a wavelet variance greater than one indicates positive spatial autocorrelation (neighboring subplots are more similar than expected).

At each spatial grain, we then tested whether the difference in spatial autocorrelation patterns across sites is explained by differences in topographic heterogeneity across sites using repeated and independent Spearman's rho correlation tests between the wavelet variance and the elevation range within plots.

2.4 Implications of field sampling error for remote sensing calibration

To assess the implications of field sampling error for remote sensing calibration, we explored the joint influence of the field plot size and of the footprint size of a hypothetical remote sensing observation on the precision of the AGB estimate. We simulated

BGD
11, 5711–5742, 2014

different field-based plot sizes and also different sizes of footprints, under the best-case scenario in which the remote sensing instrument was perfectly perceptive of AGB as measured in field plots. We modeled the remote sensing footprint as circles and the calibration plots as squares to simulate the spatial mismatch between the typical ground and remote sensing fields of view. We simulated field plots of 0.04, 0.1, 0.25, 0.5, 1, 2 and 4 ha centered in remote-sensing circular footprints of 0.5, 1, 2 and 4 ha (Fig. S2). We then calculated a measure of the mean error associated with the field plot – footprint comparison of AGB, ErrCV, for each combination of areas in which the field plot area is less than or equal to the footprint area as

$$\mathrm{ErrCV} = \frac{\sqrt{\frac{1}{N} \times \sum_{i=1}^{N} (\mathrm{AGB}_{\mathrm{footprint},\,i} - \mathrm{AGB}_{\mathrm{subplot},\,i})^2}}{\frac{1}{N} \times \sum_{i=1}^{N} \mathrm{AGB}_{\mathrm{footprint},\,i}} \quad (2)$$

where N is the number of simulations (1000 per combination), $\mathrm{AGB}_{\mathrm{footprint},\,i}$ is the AGB measured within the remote-sensing footprint (i.e. the circle) for the ith simulation, and $\mathrm{AGB}_{\mathrm{subplot},\,i}$ is the AGB measured within the field subplot for that simulation. In five of our plots (Haliburton plot and the four Ituri plots), dimensions were too small to accommodate a circular 4 ha footprint and were thus not considered to calculate ErrCV at this scale.

To illustrate how field sampling error propagates into AGB maps, we then fit calibration equations from the combination of simulated remote sensing pixels and field calibration plots. For this exercise, we simulated square remote sensing pixels of 4 ha. This spatial resolution mimics that of the BIOMASS mission's future instrument (Le Toan et al., 2011). Given the size of our field plots, we were able to simulate 60 such pixels (i.e. two per plot). Within each simulated pixel, we assumed that a single randomly located field plot was available for calibration, and we let the area of this field plot vary in size, from 0.01, 0.04, 0.25, 0.5, 1 and to 2 ha. We expect the calibration to be of poorer quality for smaller subplots than for larger ones. To assess the goodness of fit, we calculated the regression coefficients of an ordinary least squares (OLS) lin-

BGD
11, 5711–5742, 2014

ear regression between the AGB estimated in the calibration subplots of a given area and the simulated pixels. We changed the location of the subplots a thousand times and averaged the regression coefficients for each subplot size.

It is well-established in the statistical literature that random error in the independent variable, such as that which results from sampling error in field plots, leads to systematic underestimation of the OLS regression slope, a bias referred to as attenuation or regression dilution (Fuller, 1987). This phenomenon is easily understood as the OLS slope β is calculated as $\beta = \sigma^2(X,Y)/\sigma^2(X)$ where $\sigma^2(X,Y)$ is the covariance of X and Y and $\sigma^2(X)$ is the variance of X. If W is a measure of X with measurement error (that is, $W = X + \varepsilon_X$), then $\sigma^2(W) > \sigma^2(X)$ and $\sigma^2(W,Y) < \sigma^2(X,Y)$ (Mcardle, 2003). Hence, the estimate of β tends to zero as the measurement error in X increases to infinity. In practice, this means that in the presence of error in the independent variable X, the slope of an OLS regression always is underestimated, a phenomenon referred to as the dilution bias.

Several methods have been proposed to correct for this bias (Carroll and Ruppert, 1996; Frost and Thompson, 2000; Smith, 2009). The method of moments estimator (Carroll and Ruppert, 1996; Fuller, 1987) assumes that a corrected slope, β_{MM}, could be calculated from the observed slope, β, using a reliability ratio, R_{r}, with

$$\beta_{\mathrm{MM}} = \frac{\beta}{R_{\mathrm{r}}} \tag{3}$$

where

$$R_{\mathrm{r}} = \frac{\sigma^2(W) - \sigma^2(\varepsilon X)}{\sigma^2(W)} \tag{4}$$

To estimate $\sigma^2(\varepsilon X)$, the variance of the error in X, we simulated a realistic reliability study (i.e. repeated measurements in X) and estimated R_{r} using the intra-class correlation coefficient (ICC), an accurate proxy for R_{r} (Frost and Thompson, 2000). ICC

BGD
11, 5711–5742, 2014

was estimated through a one-way analysis of variance of repeated measures. We simulated "new" measurements by bootstrapping over 0.01 ha (10 m × 10 m) sub-subplots for each nested subplot (i.e. 100 bootstrapped values for each of the 60 calibration plot) and calculated the ICC considering the nested subplots as factor in the one-way analysis of variance. This approach was called "within subplot R_r". A second reliability study approach, assuming that additional subplots (i.e. replicates) were established randomly inside the 4 ha pixel, is shown in Appendix S2 and in Fig. S3, Supplement.

We also evaluated two alternatives to OLS that have the potential to produce less bias in calibration equations. First, the Reduced Major Axis (RMA) regression minimizes the sum of squared distances both horizontally (accounting for the error in X) and vertically (accounting for the error in Y). Second, the nonparametric Theil–Sen estimator, also known as Sen's slope estimator or the single median method, is the median of all the slopes determined by all pairs of sample points. Both methods have been proposed as preferred alternatives to OLS in remote sensing studies (Cohen et al., 2003; Fernandes and Leblanc, 2005; Mitchard et al., 2013a; Ryan et al., 2012).

All analyses were performed using R version 2.15.1 (R Development Core Team, 2012). The R code for the analyses is available on request from the first author.

3 Results

3.1 Sampling error in AGB across spatial scales and forest plots

The coefficient of variation for AGB at the 1-hectare scale, CV(1), varied among sites ($n = 30$) from 5.1 %, in the Haliburton plot (Canada), to 29.9 %, in the Palanan plot (Philippines), with a mean of 16.6 %, and a median of 15.2 % (Table S2). The best predictor of variation in CV(1) among plots was within-plot elevation range, that is, the difference between the highest and lowest elevation (Spearman's rho = 0.70 and $p < 10^{-4}$; Fig. 2a). Thus, topographic heterogeneity explained considerable variation in AGB heterogeneity among sites. In contrast, CV(1) was not significantly correlated

BGD
11, 5711–5742, 2014

with mean AGB (Spearman's correlation test, $p = 0.15$), and did not differ significantly among tropical ($n = 20$), subtropical ($n = 3$) and temperate ($n = 7$) forests (Kruskal–Wallis test, $p = 0.47$) or among continents (Kruskal–Wallis test: $p = 0.18$). Asian tropical field plots tended to show higher biomass heterogeneity than other tropical field plots (median CV(1) of 24.4 and 14.3 % respectively).

Regressing the logarithm of CV(s) against ln(s), we found that the exponent γ was significantly lower than 1/2 in 15 of our 30 sites, indicating significantly positive spatial autocorrelation in AGB at about half of the sites, and significantly higher than 1/2 in only two sites, the Ituri Edoro1 plot in Democratic Republic of Congo and the Paracou plot in French Guiana (Fig. 2b, Tables S2 and S3). Sites with greater elevation range showed lower fitted γ values (rho = −0.47 and $p = 0.01$). Such positive spatial autocorrelation means that extrapolation from 1 ha values under the assumption of no spatial autocorrelation will lead to a slight but systematic overestimation of CV(s) for areas (s) smaller than 1 ha, and underestimation for areas larger than 1 ha (Fig. S4).

3.2 Spatial autocorrelation in AGB at multiple spatial scales

Decomposition of the variance in AGB at different spatial grains using wavelet analysis confirmed significant spatial autocorrelation of AGB in most plots (Figs. 3a, S5 and S6). There was a general trend for negative spatial autocorrelation at spatial grains of approximately 25 to 75 m and for positive spatial autocorrelation at spatial grains of 100 m and beyond (Fig. 3a). The plots with greater topographic heterogeneity were characterized by stronger spatial autocorrelation at distances > 100 m (Fig. 3b).

3.3 Implications of field sampling error for remote sensing calibration

We quantified how field-based sampling error scales with both field plot and remote sensing footprint areas. For very small field subplots (0.1 ha and below), sampling error was due mostly to field sampling and relatively insensitive to the footprint size (Fig. 4). For subplots and footprint size of 0.5 ha and larger, subplot area and footprint area had

BGD
11, 5711–5742, 2014

similar effects on the sampling error. The error due to the spatial mismatch (circle vs. square) was much higher for small calibration plots even for a fixed ratio of the field calibration plot area to the footprint area (Fig. S8).

We explored how field-based sampling error propagate into AGB maps derived from remote sensing products. The OLS regression slope was underestimated by an average of 54 % with 0.1 ha subplots and by 37 % with 0.25 ha subplots (Fig. 5a, see examples of fits on Fig. S9). This result shows that even if though such models all correctly predict the mean AGB of the calibration plots, those with a large dilution effect (i.e. slope underestimation) would underestimate the variance in AGB, and thus systematically underestimate AGB in high AGB areas, and overestimate it in low AGB areas. Alternatives to OLS models, such as Reduced major axis (RMA) or the Theil–Sen estimator, did not fully correct for this bias (Fig. 5b). Our bias correction approach, based on bootstrapping over spatial variability within our subplots, remained too conservative, but outperformed the RMA and the Theil–Sen estimator for plots $\geq$ 0.25 ha ("within subplot R_r" in Fig. 5b, see also Appendix S2, Supplement for another reliability study approach).

4 Discussion

Given the pressing need to monitor global forest carbon stocks, ecologists and remote sensing experts need to pay careful attention to accurately quantifying the errors associated with forest carbon estimates. Our results indicate that large spatial sampling error is associated with plot sizes smaller than 0.25 ha (> 26 %). Many of the plots in standard forest inventories are much smaller than 0.25 ha and are regularly used for calibrating remote sensing models. Our findings suggest that using such small field plots to calibrate remote sensing products may lead to strong systematic biases in carbon maps.

BGD
11, 5711–5742, 2014

4.1 Quantifying sampling error in AGB

According to theory, sampling error in AGB decreases predictably with plot area. Previous studies have investigated the spatial scaling of sampling error in forest AGB (Baraloto et al., 2013; Chave et al., 2003; Holdaway et al., 2014; Keller et al., 2001; Wagner et al., 2010), but the present study is the first to generalize these findings across a wide range of forest types, both temperate and tropical. We found that the relative spatial sampling error in AGB averages ~ 16.6 % of the mean at 1 ha, and this error scales roughly with $s^{-1/2}$ where s is the plot area. Sampling error tended to be larger in hilly terrain confirming that topography is a major driver of AGB heterogeneity (e.g., de Castilho et al., 2006). This result suggests that forest biomass maps in hilly areas have larger uncertainties, and that sampling designs should take topography into account. This is an important finding given that 23 % of the world's forests are on hilly terrain (Table S4). We found no other systematic trends among continents or forest types or with mean AGB. Asian tropical forests displayed higher sampling errors than other tropical sites, but this could be explained by the larger topographic heterogeneity in our tropical Asian study sites (Table S1). This finding is no accident of our study locations; remaining old-growth tropical forests in Asia are disproportionately located in topographically complex terrain, more so than on other continents (Table S4), probably because these areas have disproportionately escaped human disturbance.

The careful quantification of spatial sampling error described here should be useful in providing guidelines for forest inventory design at the national scale, as well as in remote sensing applications (see below). It should, however, be borne in mind that we focused on errors resulting from spatial sampling and ignored other sources of error which also contribute significantly to uncertainty in AGB estimates, including errors in field measurements (e.g. diameter and height measurements or wood density attribution through floristic identification; Flores and Coomes, 2011; Larjavaara and Muller-Landau, 2013), data cleaning procedures (Muller-Landau et al., 2014), biomass allometries (Chave et al., 2004; Molto et al., 2013), and wood carbon content (Thomas

BGD
11, 5711–5742, 2014

and Martin, 2012). Finally, we focused on AGB stocks; sampling error in AGB changes is far larger due to the low frequency of AGB loss events (Chambers et al., 2013; Muller-Landau et al., 2014; Wagner et al., 2010).

4.2 Spatial autocorrelation in AGB and consequences for field sampling

The wavelet analysis revealed that most study sites displayed significant spatial autocorrelation in AGB with contrasting patterns at different spatial grains. On average, a negative autocorrelation occurred at spatial grains between 25 and 75 m. Hence, neighboring field plots ranging in size from 25 m × 25 m to 75 m × 75 m tend to provide less similar AGB estimates than plots that are separated by greater distances. Such negative autocorrelation pattern may be interpreted as the effect of spatially localized AGB changes due to treefall gap openings. For instance, in a Neotropical forest of French Guiana, van der Meer and Bongers (1996) found that the effects of large tree gaps typically occur at such spatial grains. As AGB is mainly shaped by large trees, another explanation may lie in the nature of the spatial distribution of these large trees (Lutz et al., 2013). Both competition for below- and aboveground resources among individuals and Janzen–Connell-type effects in large diameter species may generate strong density-dependence between large trees, and thus negative autocorrelation pattern in AGB. At larger distances (≥ 100 m), AGB was positively autocorrelated in many sites, and significantly so, with the degree of autocorrelation positively related to topographical heterogeneity, a feature known to influence forest structure (e.g. de Castilho et al., 2006; McEwan et al., 2011). Thus, 1 ha and larger plots are expected to be statistically more representative of a larger remote sensing footprint area than expected under the null hypothesis of no spatial correlation.

The spatial structures we found have implications for optimal plot sampling designs for forest inventories. Negative or nonexistent spatial autocorrelation at scales less than 100 m suggests that there is generally no gain in representativeness from locating multiple small plots within a small area or footprint (≤ 100 m) rather than establishing one or few larger plots in the same area. That is, because neighboring small plots are just

BGD
11, 5711–5742, 2014

as different, if not more different, from a focal plot than more distantly located small plots. Therefore expanding a single small plot provides similar or more information than adding another small plot nearby. A number of forest inventory designs use clusters of very small plots (≤ 0.04 ha); e.g., the US Forest Service Forest Inventory and Analysis program (Bechtold and Patterson, 2005). These cluster designs have distinct disadvantages for calibrating remote sensing products as their small dimensions are below the resolution of most sensors (see below), and their edge to area ratios are higher than single larger plots of the same total area. Although small plots may have practical advantages in field sampling, these should be carefully weighed against the above-mentioned disadvantages.

In contrast, significant spatial autocorrelation of AGB at scales larger than 100 m suggests that many intermediate scale plots of ~ 0.25–1 ha will better approximate the mean AGB of a landscape than fewer large plots having the same total surveyed area. This would be especially true if such a sampling design was stratified according to topography. However, as discussed below, small plots may lead to strong systematic biases and errors when used individually for calibrating remote sensing products of larger resolution.

4.3 Field sampling error and remote sensing of carbon stocks

As expected, sampling error depends both on field plot area and on the size of the remote sensing footprint. However, when field subplots were very small (0.1 ha and below), the uncertainty was due mostly to field sampling, and was relatively insensitive to the footprint area. For subplots and footprints of 0.5–4.0 ha, both subplot and footprint areas have strong effects on sampling error. We also found that error was much lower for large calibration plots even when the same ratio of calibration plot area to footprint area was maintained. This reflects decreasing edge-to-area ratios for larger area, which also provide other advantages to larger plots (Mascaro et al., 2011; see also Zolkos et al., 2013).

BGD
11, 5711–5742, 2014

Our analyses show that field-sampling strategy may result in a serious bias in model calibration of remote sensing products. When this bias is present, inversion models return AGB values that are regressed to the mean of the calibration plots (Fig. 5a), and thus underestimate the true spatial AGB variance. For instance, in a recent study that used 112 circular 0.13 ha plots to calibrate L-band radar products (Carreiras et al., 2012), the slope of an OLS regression was found to be underestimated by 86 % and the final AGB map displayed a much lower variance than the global map produced by Saatchi et al. (2011). The dilution bias is independent of the number of calibration plots, and it depends only on the size (and thus sampling error) of these plots. In addition such an inversion model estimates is expected to estimate the mean AGB of the sampling plots correctly (Fig. 5a), but the mean of a biomass map may still seriously be biased, unless calibration plots are truly representative of the AGB for the mapped area.

We tested several alternative approaches to OLS regression and found that the best way to diminish this bias is to bootstrap over spatial variability within subplots and to correct the estimated slope using these simulated "replicates". Some remote sensing studies have argued that alternative to OLS regression such as RMA or the Theil–Sen estimator are good alternatives to OLS regression when errors occur in X (Cohen et al., 2003; Fernandes and Leblanc, 2005; Mitchard et al., 2013a; Ryan et al., 2012). Here, we showed that these alternatives do not resolve the dilution bias and still provide strongly biased products. Furthermore, the use of RMA is contentious (Carroll and Ruppert, 1996; Smith, 2009), especially if the primary purpose of the regression equation is prediction (Legendre and Legendre, 1998). Sampling error propagation in other empirical calibration approaches should be carefully explored in the future.

The best way to avoid the dilution bias is to use calibration plots covering entire remote sensing pixels. For remote sensing tools with a resolution on the order of 4 ha, such as the planned BIOMASS mission, it is realistic to invest in a network of similarly-sized field calibration plots. Though such field sampling is expensive, it would greatly improve the basis for mapping forest biomass. An alternative is to calibrate coarse-resolution remote sensing with higher-resolution remote sensing such as airborne Li-

BGD
11, 5711–5742, 2014

DAR, which is itself well calibrated with smaller plots (Mascaro et al., 2011). In these cases, care must be taken that errors and uncertainties are carefully and appropriately propagated through the two-stage calibration to the final map (Asner et al., 2013).

5 Conclusion

Accurate measurements of forest carbon stocks are critical to reduce uncertainties in the global carbon budget. However, uncertainty associated with forest carbon map products, from either field based and/or remote-sensing approaches, has been overlooked in most studies. In this paper, we used a large-scale global dataset to illustrate that high spatial variability in AGB within forested sites leads to large sampling error at standard plot sizes (< 0.25 ha). Topographical heterogeneity is a major source of sampling error and should be thus explicitly accounted for in future sampling scheme. We also show that remote sensing products that rely on field data for calibration may be highly biased if field-sampling error is large. Such biases have previously been ignored by the remote sensing community and, as we show, can only be partially corrected by statistical methods alone. Overall, our results strongly suggest that more large forest plots (> 0.25 ha) are needed to enable accurate calibration of remote sensing estimates of forest carbon. We hope that this contribution will stimulate further work on field sampling error propagation to remote sensing products and that future studies will pay more careful attention to field sampling strategies.

Supplementary material related to this article is available online at http://www.biogeosciences-discuss.net/11/5711/2014/bgd-11-5711-2014-supplement.pdf.

Acknowledgements. We are grateful to all the people, institutions, foundations, and funding bodies that have contributed to the collection of the large plot datasets (http://www.ctfs.si.edu/

BGD
11, 5711–5742, 2014

group/Partners/Collaborating+Institutions for the CTFS plots), including the staff members and central office of the Amacayacu National Natural Park of Colombia. We sincerely thank Erika Gonzalez and Sandeep Pulla for their help with analyses for the SCBI and Mudumalai plots, respectively. Financial support for the analyses presented here was provided by the CNES (postdoctoral grant to MRM), the National Science Foundation (DEB #1046113), and two "Investissement d'Avenir" grants managed by Agence Nationale de la Recherche (CEBA: ANR-10-LABX-25-01; TULIP: ANR-10-LABX-0041).

References

Abdalati, W., Zwally, H. J., Bindschadler, R., Csatho, B., Farrell, S. L., Fricker, H. A., Harding, D., Kwok, R., Lefsky, M., Markus, T., Marshak, A., Neumann, T., Palm, S., Schutz, B., Smith, B., Spinhirne, J., and Webb, C.: The ICESat-2 Laser Altimetry Mission, Proceedings of the IEEE, 98, 735–751, doi:10.1109/JPROC.2009.2034765, 2010.

Asner, G. P., Powell, G. V. N., Mascaro, J., Knapp, D. E., Clark, J. K., Jacobson, J., Kennedy-Bowdoin, T., Balaji, A., Paez-Acosta, G., Victoria, E., Secada, L., Valqui, M., and Hughes, R. F.: High-resolution forest carbon stocks and emissions in the Amazon, P. Natl. Acad. Sci. USA, 107, 16738–16742, doi:10.1073/pnas.1004875107, 2010.

Asner, G. P., Mascaro, J., Anderson, C., Knapp, D. E., Martin, R. E., Kennedy-Bowdoin, T., Breugel, M. van, Davies, S., Hall, J. S., Muller-Landau, H. C., Potvin, C., Sousa, W., Wright, J., and Bermingham, E.: High-fidelity national carbon mapping for resource management and REDD+, Carbon Balance and Management, 8, 1–14, doi:10.1186/1750-0680-8-7, 2013.

Baccini, A., Friedl, M. A., Woodcock, C. E., and Zhu, Z.: Scaling field data to calibrate and validate moderate spatial resolution remote sensing models, Photogramm. Eng. Rem. S., 73, 945–954, 2007.

Baccini, A., Goetz, S. J., Walker, W. S., Laporte, N. T., Sun, M., Sulla-Menashe, D., Hackler, J., Beck, P. S. A., Dubayah, R., Friedl, M. A., Samanta, S., and Houghton, R. A.: Estimated carbon dioxide emissions from tropical deforestation improved by carbon-density maps, Nature Climate Change, 2, 182–185, doi:10.1038/nclimate1354, 2012.

Baraloto, C., Molto, Q., Rabaud, S., Hérault, B., Valencia, R., Blanc, L., Fine, P. V. A., and Thompson, J.: Rapid simultaneous estimation of aboveground biomass and tree diversity

BGD
11, 5711–5742, 2014

across neotropical forests: a comparison of field inventory methods, Biotropica, 45, 288–298, doi:10.1111/btp.12006, 2013.
Bechtold, W. A. and Patterson, P. L.: The Enhanced Forest Inventory and Analysis Program: National Sampling Design and Estimation Procedures, US Department of Agriculture Forest Service, Southern Research Station, available at: http://www.srs.fs.usda.gov/pubs/gtr/gtr_srs080/gtr_srs080 (last access: 18 September 2013), 2005.
Bontemps, S., Defourny, P., Van Bogaert, E., Arino, O., Kalogirou, V., and Ramos Perez, J.: GLOBCOVER 2009 Products Description and Validation Report, available at: https://globcover.s3.amazonaws.com/LandCover2009/GLOBCOVER2009_Validation_Report_1.0.pdf, 2011.
Carreiras, J. M. B., Vasconcelos, M. J., and Lucas, R. M.: Understanding the relationship between aboveground biomass and ALOS PALSAR data in the forests of Guinea-Bissau (West Africa), Remote Sens. Environ., 121, 426–442, doi:10.1016/j.rse.2012.02.012, 2012.
Carroll, R. J. and Ruppert, D.: The use and misuse of orthogonal regression in linear errors-in-variables models, Am. Stat., 50, 1–6, doi:10.1080/00031305.1996.10473533, 1996.
Chambers, J. Q., Negron-Juarez, R. I., Marra, D. M., Vittorio, A. D., Tews, J., Roberts, D., Ribeiro, G. H. P. M., Trumbore, S. E., and Higuchi, N.: The steady-state mosaic of disturbance and succession across an old-growth Central Amazon forest landscape, P. Natl. Acad. Sci. USA, 110, 3949–3954, doi:10.1073/pnas.1202894110, 2013.
Chave, J., Condit, R., Lao, S., Caspersen, J. P., Foster, R. B., and Hubbell, S. P.: Spatial and temporal variation of biomass in a tropical forest: results from a large census plot in Panama, J. Ecol., 91, 240–252, 2003.
Chave, J., Condit, R., Aguilar, S., Hernandez, A., Lao, S., and Perez, R.: Error propagation and scaling for tropical forest biomass estimates, Philos. T. R. Soc. B, 359, 409–420, 2004.
Chave, J., Condit, R., Muller-Landau, H. C., Thomas, S. C., Ashton, P. S., Bunyavejchewin, S., Co, L. L., Dattaraja, H. S., Davies, S. J., Esufali, S., Ewango, C. E. N., Feeley, K. J., Foster, R. B., Gunatilleke, N., Gunatilleke, S., Hall, P., Hart, T. B., Hernández, C., Hubbell, S. P., Itoh, A., Kiratiprayoon, S., LaFrankie, J. V., Loo de Lao, S., Makana, J.-R., Noor, M. N. S., Kassim, A. R., Samper, C., Sukumar, R., Suresh, H. S., Tan, S., Thompson, J., Tongco, M. D. C., Valencia, R., Vallejo, M., Villa, G., Yamakura, T., Zimmerman, J. K., and Losos, E. C.: Assessing evidence for a pervasive alteration in tropical tree communities, PLoS Biol., 6, 3e45 doi:10.1371/journal.pbio.0060045, 2008.

BGD
11, 5711–5742, 2014

Cohen, W. B., Maiersperger, T. K., Gower, S. T., and Turner, D. P.: An improved strategy for regression of biophysical variables and Landsat ETM+ data, Remote Sens. Environ., 84, 561–571, doi:10.1016/S0034-4257(02)00173-6, 2003.

Condit, R.: Research in large, long-term tropical forest plots, Trends Ecol. Evol., 10, 18–22, 1995.

Condit, R.: Tropical Forest Census Plots: Methods and Results from Barro Colorado Island, Panama and a Comparison with Other Plots, Springer, Berlin, Germany, 1998.

De Castilho, C. V., Magnusson, W. E., de Araújo, R. N. O., Luizão, R. C. C., Luizão, F. J., Lima, A. P., and Higuchi, N.: Variation in aboveground tree live biomass in a central Amazonian Forest: effects of soil and topography, Forest Ecol. Manag., 234, 85–96, doi:10.1016/j.foreco.2006.06.024, 2006.

Fernandes, R. and Leblanc, S.: Parametric (modified least squares) and non-parametric (Theil–Sen) linear regressions for predicting biophysical parameters in the presence of measurement errors, Remote Sens. Environ., 95, 303–316, doi:10.1016/j.rse.2005.01.005, 2005.

Flores, O. and Coomes, D. A.: Estimating the wood density of species for carbon stock assessments, Methods in Ecology and Evolution, 2, 214–220, doi:10.1111/j.2041-210X.2010.00068.x, 2011.

Frost, C. and Thompson, S. G.: Correcting for regression dilution bias: comparison of methods for a single predictor variable, J. Roy. Stat. Soc. A Sta., 163, 173–189, 2000.

Fuller, W. A.: Measurement Error Models, John Wiley, New York, 1987.

Gibbs, H. K., Brown, S., Niles, J. O., and Foley, J. A.: Monitoring and estimating tropical forest carbon stocks: making REDD a reality, Environ. Res. Lett., 2, 045023, doi:10.1088/1748-9326/2/4/045023, 2007.

Goetz, S. and Dubayah, R.: Advances in remote sensing technology and implications for measuring and monitoring forest carbon stocks and change, Carbon Management, 2, 231–244, 2011.

Gonzalez, P., Asner, G. P., Battles, J. J., Lefsky, M. A., Waring, K. M., and Palace, M.: Forest carbon densities and uncertainties from Lidar, QuickBird, and field measurements in California, Remote Sens. Environ., 114, 1561–1575, 2010.

Holdaway, R. J., McNeill, S. J., Mason, N. W., and Carswell, F. E.: Propagating uncertainty in plot-based estimates of forest carbon stock and carbon stock change, Ecosystems, 1–14, 2014.

BGD
11, 5711–5742, 2014

Keller, M., Palace, M., and Hurtt, G.: Biomass estimation in the Tapajos National Forest, Brazil: examination of sampling and allometric uncertainties, Forest Ecol. Manag., 154, 371–382, doi:10.1016/S0378-1127(01)00509-6, 2001.

Larjavaara, M. and Muller-Landau, H. C.: Measuring tree height: a quantitative comparison of two common field methods in a moist tropical forest, Methods in Ecology and Evolution, 4, 793–801, doi:10.1111/2041-210X.12071, 2013.

Le Toan, T., Quegan, S., Davidson, M. W. J., Balzter, H., Paillou, P., Papathanassiou, K., Plummer, S., Rocca, F., Saatchi, S., Shugart, H., and Ulander, L.: The BIOMASS mission: mapping global forest biomass to better understand the terrestrial carbon cycle, Remote Sens. Environ., 115, 2850–2860, doi:10.1016/j.rse.2011.03.020, 2011.

Legendre, P. and Legendre, L.: Numerical Ecology, 2nd edn., Elsevier Science BV, Amsterdam, 1998.

Lewis, S. L., Lopez-Gonzalez, G., Sonké, B., Affum-Baffoe, K., Baker, T. R., Ojo, L. O., Phillips, O. L., Reitsma, J. M., White, L., Comiskey, J. A., K, M.-N. D., Ewango, C. E. N., Feldpausch, T. R., Hamilton, A. C., Gloor, M., Hart, T., Hladik, A., Lloyd, J., Lovett, J. C., Makana, J.-R., Malhi, Y., Mbago, F. M., Ndangalasi, H. J., Peacock, J., Peh, K. S.-H., Sheil, D., Sunderland, T., Swaine, M. D., Taplin, J., Taylor, D., Thomas, S. C., Votere, R., and Wöll, H.: Increasing carbon storage in intact African tropical forests, Nature, 457, 1003–1006, doi:10.1038/nature07771, 2009.

Losos, E. C. and Leigh, E. G.: The growth of a tree plot network, in: Tropical Forest Diversity and Dynamism: Findings from a Large-Scale Plot Network, 3–7, 2004.

Lutz, J. A., Larson, A. J., Freund, J. A., Swanson, M. E., and Bible, K. J.: The importance of large-diameter trees to forest structural heterogeneity, PLOS ONE, 8, e82784, doi:10.1371/journal.pone.0082784, 2013.

Malhi, Y., Wood, D., Baker, T. R., Wright, J., Phillips, O. L., Cochrane, T., Meir, P., Chave, J., Almeida, S., Arroyo, L., Higuchi, N., Killeen, T. J., Laurance, S. G., Laurance, W. F., Lewis, S. L., Monteagudo, A., Neill, D. A., Vargas, P. N., Pitman, N. C. A., Quesada, C. A., Salomão, R., Silva, J. N. M., Lezama, A. T., Terborgh, J., Martínez, R. V., and Vinceti, B.: The regional variation of aboveground live biomass in old-growth Amazonian forests, Glob. Change Biol., 12, 1107–1138, doi:10.1111/j.1365-2486.2006.01120.x, 2006.

Mascaro, J., Detto, M., Asner, G. P., and Muller-Landau, H. C.: Evaluating uncertainty in mapping forest carbon with airborne LiDAR, Remote Sens. Environ., 115, 3770–3774, doi:10.1016/j.rse.2011.07.019, 2011.

BGD
11, 5711–5742, 2014

McArdle, B. H.: Lines, models, and errors: regression in the field, Limnol. Oceanogr., 48, 1363–1366, 2003.

McEwan, R. W., Lin, Y.-C., Sun, I.-F., Hsieh, C.-F., Su, S.-H., Chang, L.-W., Song, G.-Z. M., Wang, H.-H., Hwong, J.-L., Lin, K.-C., Yang, K.-C., and Chiang, J.-M.: Topographic and biotic regulation of aboveground carbon storage in subtropical broad-leaved forests of Taiwan, Forest Ecol. Manag., 262, 1817–1825, doi:10.1016/j.foreco.2011.07.028, 2011.

Mermoz, S., Le Toan, T., Villard, L., Réjou-Méchain, M., and Seifert-Granzin, J.: Biomass assessment in the Cameroon savanna using ALOS PALSAR data, Remote Sens. Environ., in press, 2014.

Miles, L. and Kapos, V.: Reducing greenhouse gas emissions from deforestation and forest degradation: global land-use implications, Science, 320, 1454–1455, doi:10.1126/science.1155358, 2008.

Mitchard, E. T. A., Meir, P., Ryan, C. M., Woollen, E. S., Williams, M., Goodman, L. E., Mucavele, J. A., Watts, P., Woodhouse, I. H., and Saatchi, S. S.: A novel application of satellite radar data: measuring carbon sequestration and detecting degradation in a community forestry project in Mozambique, Plant Ecology & Diversity, 6, 159–170, doi:10.1080/17550874.2012.695814, 2013a.

Mitchard, E. T. A., Saatchi, S. S., Baccini, A., Asner, G. P., Goetz, S. J., Harris, N., and Brown, S.: Uncertainty in the spatial distribution of tropical forest biomass: a comparison of pan-tropical maps, Carb Bal Manage, available at: http://www.biomedcentral.com/content/pdf/1750-0680-8-10.pdf (last access: 28 January 2014), 2013b.

Molto, Q., Rossi, V., and Blanc, L.: Error propagation in biomass estimation in tropical forests, Methods in Ecology and Evolution, 4, 175–183, doi:10.1111/j.2041-210x.2012.00266.x, 2013.

Muller-Landau, H. C., Detto, M., Chisholm, R. A., Hubbel, S. P., and Condit, R.: Detecting and projecting changes in forest biomass from plot data, in: Forests and Global Change, edited by: Coomes, D. A. and Burslem, D., available at: http://books.google.fr/books?hl=fr&lr=&id=QHdYAgAAQBAJ&oi=fnd&pg=PA381&dq=detecting+and+projecting+changes+biomass+condit+detto&ots=HSziWpN2aa&sig=nufRDPI5gMMHYibmapP2b_4-4Yc (last access: 22 December 2013), 381–415, 2014.

Pan, Y., Birdsey, R. A., Fang, J., Houghton, R., Kauppi, P. E., Kurz, W. A., Phillips, O. L., Shvidenko, A., Lewis, S. L., and Canadell, J. G.: A large and persistent carbon sink in the world's forests, Science, 333, 988–993, 2011.

BGD
11, 5711–5742, 2014

Percival, D. P.: On estimation of the wavelet variance, Biometrika, 82, 619–631, doi:10.1093/biomet/82.3.619, 1995.

Phillips, O. L., Aragao, L. E. O. C., Lewis, S. L., Fisher, J. B., Lloyd, J., Lopez-Gonzalez, G., Malhi, Y., Monteagudo, A., Peacock, J., Quesada, C. A., van der Heijden, G., Almeida, S., Amaral, I., Arroyo, L., Aymard, G., Baker, T. R., Banki, O., Blanc, L., Bonal, D., Brando, P., Chave, J., de Oliveira, A. C. A., Cardozo, N. D., Czimczik, C. I., Feldpausch, T. R., Freitas, M. A., Gloor, E., Higuchi, N., Jimenez, E., Lloyd, G., Meir, P., Mendoza, C., Morel, A., Neill, D. A., Nepstad, D., Patino, S., Penuela, M. C., Prieto, A., Ramirez, F., Schwarz, M., Silva, J., Silveira, M., Thomas, A. S., Steege, H. T., Stropp, J., Vasquez, R., Zelazowski, P., Davila, E. A., Andelman, S., Andrade, A., Chao, K.-J., Erwin, T., Di Fiore, A., Honorio C., E., Keeling, H., Killeen, T. J., Laurance, W. F., Cruz, A. P., Pitman, N. C. A., Vargas, P. N., Ramirez-Angulo, H., Rudas, A., Salamao, R., Silva, N., Terborgh, J., and Torres-Lezama, A.: Drought Sensitivity of the Amazon Rainforest, Science, 323, 1344–1347, doi:10.1126/science.1164033, 2009.

R Development Core Team: R: a Language and Environment for Statistical Computing, Vienna, Austria, 2012.

Ranneby, B., Cruse, T., Hägglund, B., Jonasson, H., and Swärd, J.: Designing a new national forest survey for Sweden, available at: http://pub.epsilon.slu.se/id/eprint/4634 (last access: 18 September 2013), 1987.

Ryan, C. M., Hill, T., Woollen, E., Ghee, C., Mitchard, E., Cassells, G., Grace, J., Woodhouse, I. H., and Williams, M.: Quantifying small-scale deforestation and forest degradation in African woodlands using radar imagery, Glob. Change Biol., 18, 243–257, doi:10.1111/j.1365-2486.2011.02551.x, 2012.

Saatchi, S. S., Harris, N. L., Brown, S., Lefsky, M., Mitchard, E. T. A., Salas, W., Zutta, B. R., Buermann, W., Lewis, S. L., Hagen, S., Petrova, S., White, L., Silman, M., and Morel, A.: Benchmark map of forest carbon stocks in tropical regions across three continents, P. Natl. Acad. Sci. USA, 108, 9899–9904, doi:10.1073/pnas.1019576108, 2011.

Schnitzer, S. A., Mangan, S. A., Dalling, J. W., Baldeck, C. A., Hubbell, S. P., Ledo, A., Muller-Landau, H., Tobin, M. F., Aguilar, S., and Brassfield, D.: Liana abundance, diversity, and distribution on Barro Colorado Island, Panama, PLOS ONE, 7, e52114, doi:10.1371/journal.pone.0052114, 2012.

Smith, R. J.: Use and misuse of the reduced major axis for line-fitting, Am. J. Phys. Anthropol., 140, 476–486, doi:10.1002/ajpa.21090, 2009.

BGD
11, 5711–5742, 2014

Thomas, S. C. and Martin, A. R.: Carbon content of tree tissues: a synthesis, Forests, 3, 332–352, doi:10.3390/f3020332, 2012.

Van der Meer, P. J. and Bongers, F.: Patterns of tree-fall and branch-fall in a tropical rain forest in french guiana, J. Ecol., 84, 19–29, doi:10.2307/2261696, 1996.

Wagner, F., Rutishauser, E., Blanc, L., and Herault, B.: Effects of plot size and census interval on descriptors of forest structure and dynamics, Biotropica, 42, 664–671, doi:10.1111/j.1744-7429.2010.00644.x, 2010.

Wulder, M. A., White, J. C., Nelson, R. F., Næsset, E., Ørka, H. O., Coops, N. C., Hilker, T., Bater, C. W., and Gobakken, T.: Lidar sampling for large-area forest characterization: a review, Remote Sens. Environ., 121, 196–209, doi:10.1016/j.rse.2012.02.001, 2012.

Zolkos, S. G., Goetz, S. J., and Dubayah, R.: A meta-analysis of terrestrial aboveground biomass estimation using lidar remote sensing, Remote Sens. Environ., 128, 289–298, doi:10.1016/j.rse.2012.10.017, 2013.

BGD
11, 5711–5742, 2014

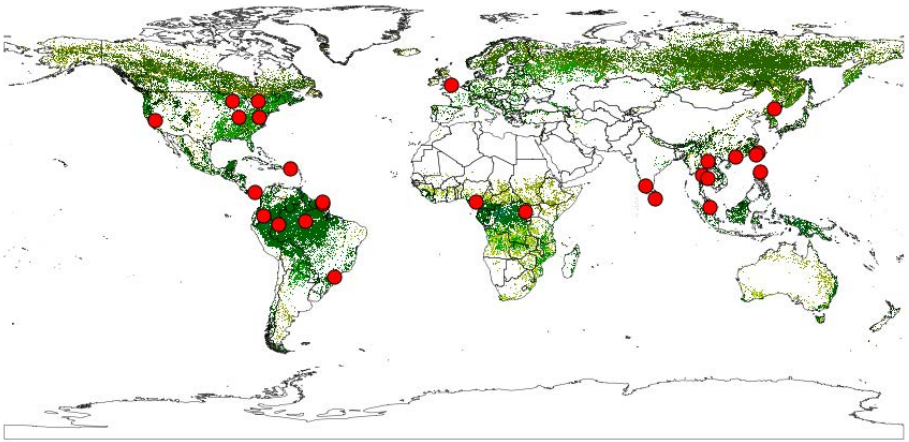

Fig. 1. Study sites. Geographical distribution of the 30 sites (red points) included in the present study. Note that the four sites at Ituri (Democratic Republic of Congo) are represented by a single dot due to their proximity. Forest distribution is shown in green (from Bontemps et al., 2011). Details on study sites are provided in Table S1.

BGD
11, 5711–5742, 2014

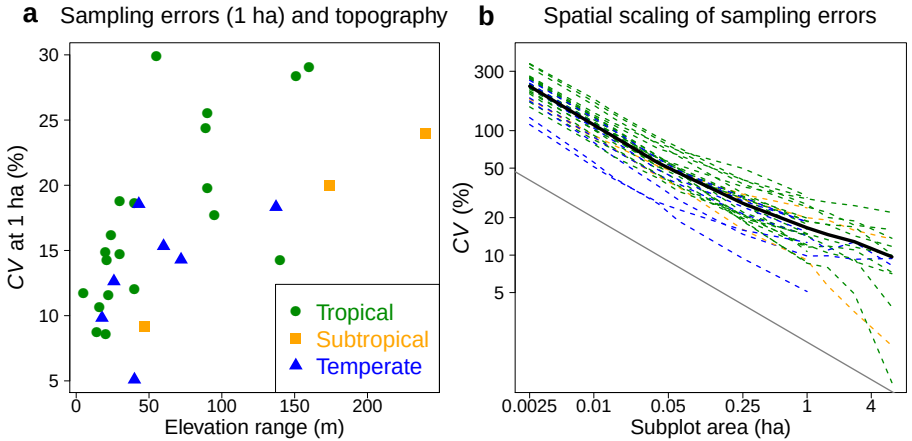

Fig. 2. Sampling error as a function of topographic heterogeneity and of spatial scale. **(a)** represents the coefficient of variation for AGB at the 1 hectare scale, CV(1), as a function of elevation range (the difference between highest and lowest altitude in the plot) for each of the plots. **(b)** shows the spatial scaling of sampling error in AGB within sites, from 0.0025 ha to 6.25 ha. The coefficients of variation (CV(s)) of AGB for individual sites (dotted lines) and means over all sites (solid black line) as a function of subplot area, are compared with the theoretical slope of −0.5 (on these log–log axes), in the absence of spatial autocorrelation in AGB (solid grey line). Separate graphs for each individual site are provided in Fig. S4 and separate graphs according to the topographic heterogeneity are provided in Fig. S5.

BGD
11, 5711–5742, 2014

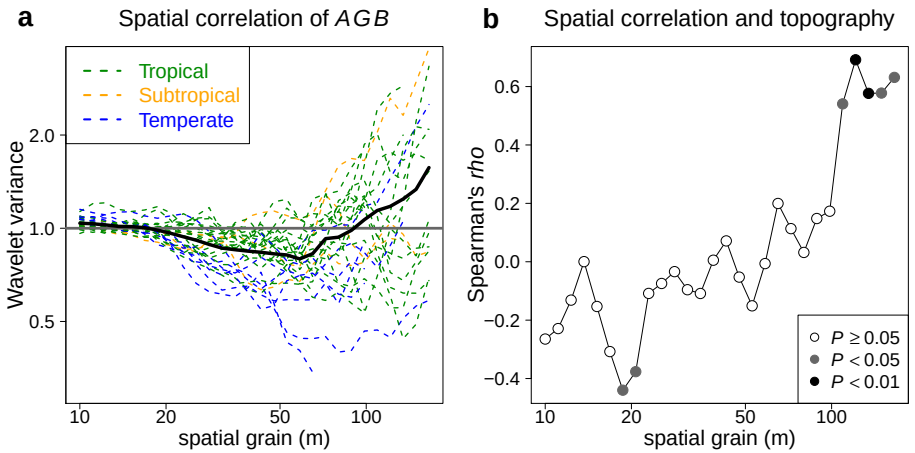

Fig. 3. Scale-dependent patterns of spatial autocorrelation in AGB and relationship to topographic heterogeneity. **(a)** shows the spatial grain-dependent patterns of spatial autocorrelation in AGB as reflected in the wavelet variance as a function of spatial grain for each site (dashed lines), together with the ensemble average across all sites (solid black line). In the absence of spatial autocorrelation the wavelet variance is expected to equal one irrespective of spatial grain (solid grey line). A wavelet variance lower than one at a given spatial grain (e.g., the average for 25–75 m) indicates overdispersion at that spatial grain, while a wavelet variance greater than one (e.g., the average for > 100 m) indicates clustering at that spatial grain. **(b)** shows the Spearman's *rho* correlation of the elevation range with the wavelet variance among sites, as a function of spatial grain at which the wavelet variance is computed. *P* values of the Spearman's rho correlation tests are provided within the panel and indicate that significant negative correlations between the wavelet variance and the topographic relief occur at spatial grains of approximately 20 m, while strong and significant positive correlations occur at spatial grains above 100 m. Separate graphs for each site, with confidence intervals for the null hypothesis of no spatial correlation, are shown in Fig. S6; separate graphs with sites grouped by topographic heterogeneity are shown in Fig. S7.

BGD
11, 5711–5742, 2014

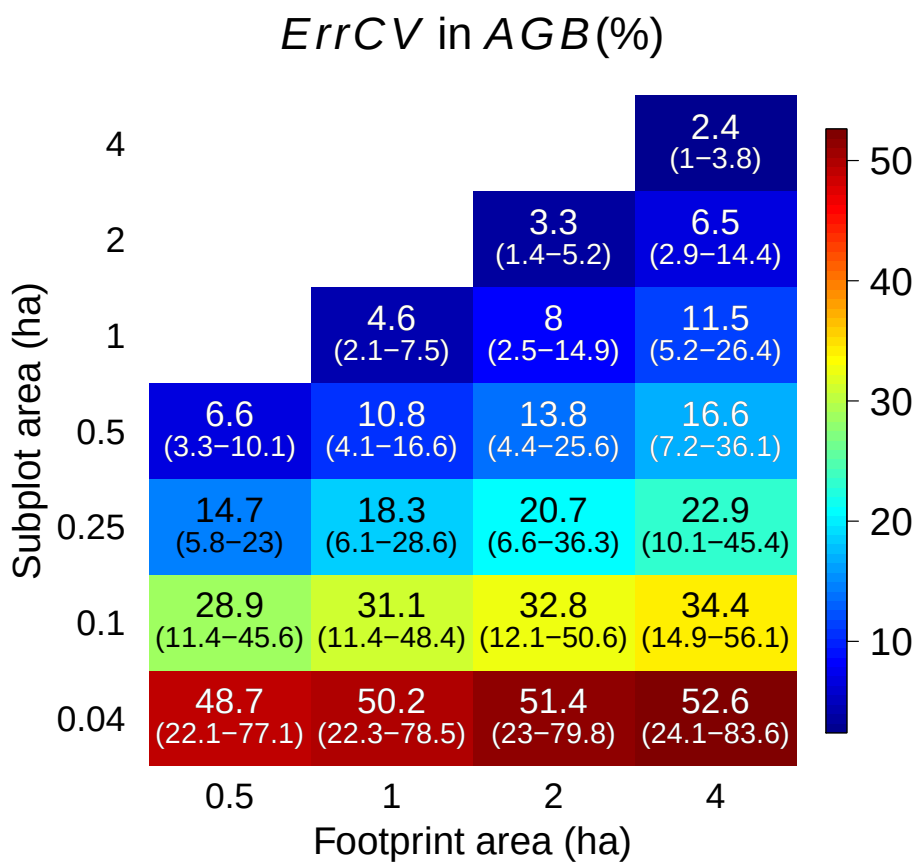

Fig. 4. Expected errors when the calibration/validation plots and the remote sensing footprint differ in shape and size. The remote sensing footprint is assumed circular, and subplots are assumed to be square to simulate the spatial mismatch between the remote sensing signal and the calibration plot. The mean ErrCV in AGB estimates across all sites ($n = 30$) is given within the figure and the range of ErrCV across sites is given in parentheses below the mean.

BGD
11, 5711–5742, 2014

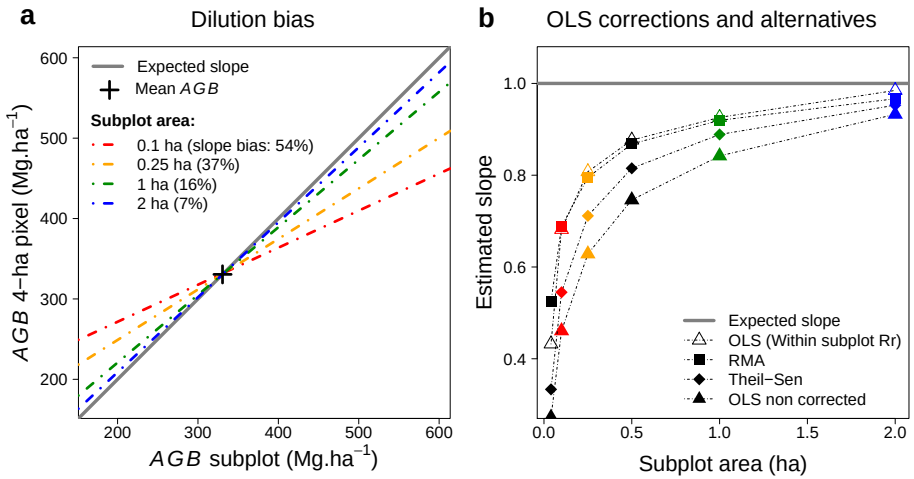

Fig. 5. Propagation of field sampling error to remote sensing products: the dilution bias. **(a)** illustrates the mean regression lines obtained from an OLS linear regression between the AGB estimated within 4 ha pixels randomly established in large plots ($n = 60$, dependent variable) and variable-size subplots located within these pixels (independent variable). Different subplot areas were simulated (see key). An unbiased estimated slope should be equal to one. Slope dilution biases associated with each subplot area are provided in parentheses. All the lines cross at the mean AGB over all sites showing that the regression correctly predicts the mean AGB of the calibration plots. However, the smaller the subplot, the more regressed to the mean the predictions. **(b)** shows how the estimated slope varies under different potential correction methods (see key) and with subplot area, compared with the true slope of one (solid grey line).

BGD
11, 5711–5742, 2014

SUPPLEMENTARY MATERIAL

APPENDICES

Appendix S1: Description of the wavelet analysis

The wavelet transform is defined as

$$W_f(\boldsymbol{b}, s, \theta) = s^{-1} \int f(\boldsymbol{x}') \phi_s^*(\boldsymbol{x}' - \boldsymbol{b}) d\boldsymbol{x}'$$

where $f(\boldsymbol{x})$ is the raster of the *AGB* at the smallest field resolution (5 m x 5 m pixel), $\phi_s^*(\boldsymbol{x} - \boldsymbol{b})$ is the complex conjugate of the scaled and translated mother wavelet, s is the scale at which the transform is applied, and $\boldsymbol{b}$ is the translation vector. The convolution is efficiently computed using fast Fourier routines. We used an isotropic Morlet wavelet, with Fourier transform given by

$$\hat{\phi}_s = \frac{s}{c_\phi} \exp\left[-\frac{1}{2} \left(s\boldsymbol{k} - k_0 \right)^2 \right]$$

The functions ∅ are essentially band-pass filters whose properties depend on the associated scaling parameter, s. They enable a focus on features of the process whose detail matches their scale parameters, i.e., broad features for large s and fine features for small s. We compute the wavelet variance or spectrum, $S_{ff}(s)$, as

$$S_{ff}(s, \theta) = \int_A |W_f(\boldsymbol{b}, s)|^2 \, d\boldsymbol{b}$$

Appendix S2: A second reliability study approach

In this reliability study, we assumed that additional subplots (i.e. replicates) of 0.04 ha (n=19), 0.1 ha (n=9), 0.25 ha (n=4), 0.5 ha (n=2), 1 ha (n=1) and 2 ha (n=1) were established randomly inside the 4-ha pixel. The numbers of additional subplots were chosen to be realistic and increasing these numbers did not affect the results (not shown). Two cases were simulated: additional subplots did not overlap each other or with the original subplot ("Replicate *Rr*") or additional subplots were allowed to overlap each other or the original subplot ("Replicate *Rr* Overlap"). The original subplot and the replicates were then used to calculate the ICC considering the 4-ha pixel as factor in the one-way analysis of variance (see methods). Results showed that "Replicate *Rr*" tended to overestimate the correction needed for all subplot areas and "Replicate *Rr* Overlap" overestimated the correction needed for small subplot but underestimate the correction for larger subplot area (Fig. S3). In all cases, these corrections did not outperform the "within subplot *Rr*" bootstrap approach for a given surveyed area.

FIGURES

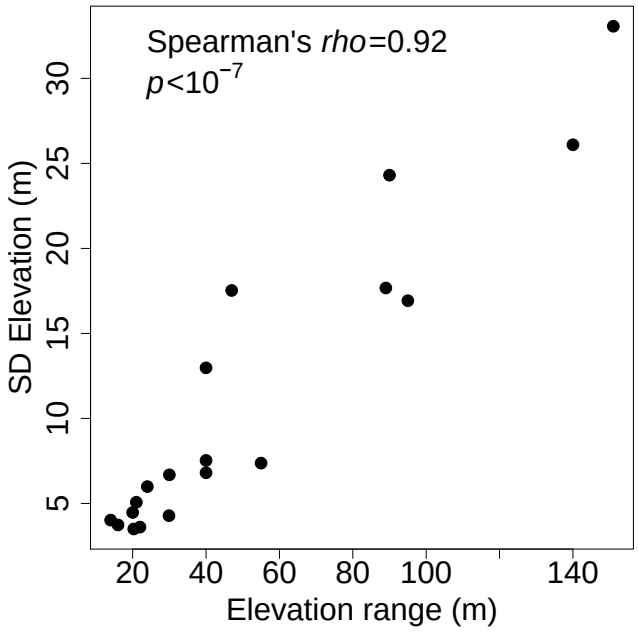

Figure S1. Relation between the range of elevation and the mean standard deviation (SD) of elevation within 1-ha subplots in 19 study sites. Because elevation range is dependent not only upon topographical heterogeneity but also on plot size, we examined how elevation range correlated with a plot-size-independent measure of topographical heterogeneity, specifically the mean standard deviation of elevation within 1-ha subplots. Pearson's correlation test results are given within the panel. The SD of elevation was calculated for each discrete 1-ha within each plot from elevation maps of 5 to 20 m resolution, and then averaged over 1-ha subplots within each plot (the SD of elevation was almost insensitive to the resolution grain size, result not shown). All sites for which elevation maps were available were included in this analysis (Amacayacu, Barro Colorado Island, Fushan, Haliburton, Huai Kha Khaeng, Ituri Edoro1, Ituri Edoro2, Ituri Lenda1, Ituri Lenda2, Korup, Luquillo, Manaus, Mudumalai, Nouragues, Palanan, Paracou, Pasoh, Sinharaja, Yasuni).

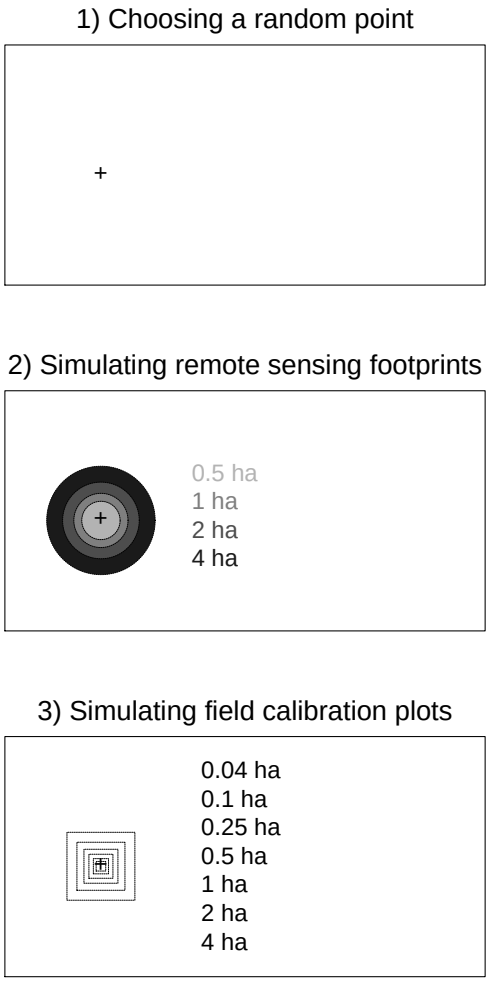

Figure S2. **Schematic representation of the method used to assess the expected errors when the calibration/validation plots and the remote sensing footprint differ in shape and size** 1) A center of both remote sensing footprint and subplot was chosen randomly in a subarea of the whole plot so that the disk representing the footprint, and the squares representing the subplots, are fully inside the plot for footprint and subplot areas examined. 2) $AGB_{footprint}$ is calculated within circular footprints (simulating the remote sensing signal) and 3) $AGB_{subplot}$ is calculated within square subplots (simulating the calibration/validation plots nested and centered within the circular footprints). The coefficient of variation is then calculated for each combination in which the subplot area is less than the footprint area as:

$$CV = \sqrt{1/\mathrm{N} \times \sum_{\mathrm{i}=1}^{\mathrm{N}} \left(AGB_{footprint} - AGB_{subplot}\right)^2} \Big/ 1/\mathrm{N} \times \sum_{\mathrm{i}=1}^{\mathrm{N}} AGB_{footprint}$$

We replicated this procedure 1000 times, and averaged the *CV* for every combination of scale within each plot.

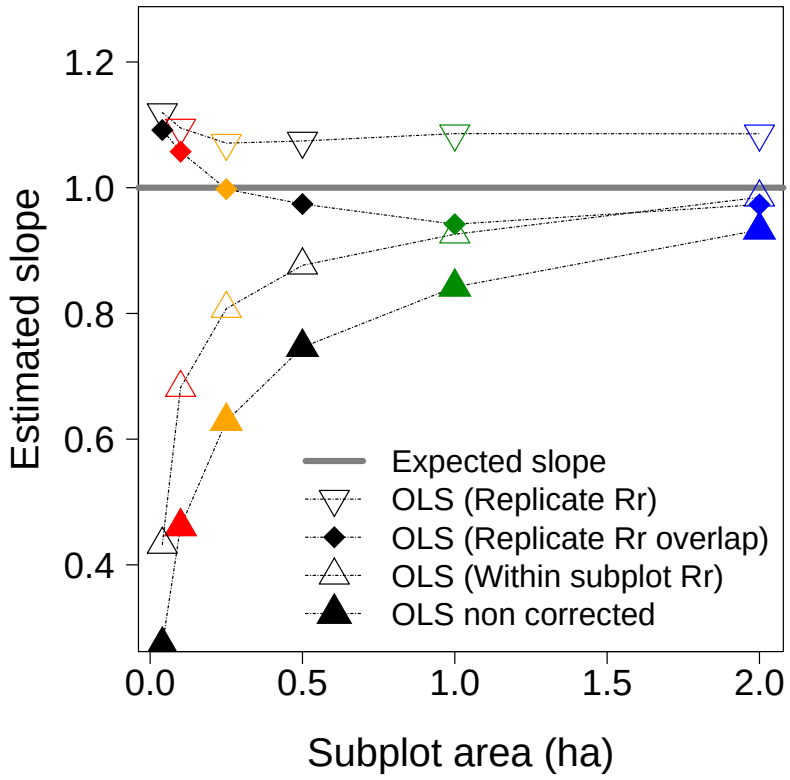

Figure S3. Additional reliability study approach assuming that additional subplots were established randomly inside the 4-ha pixel. See Appendix S2 and figure 5 of the main manuscript for details.

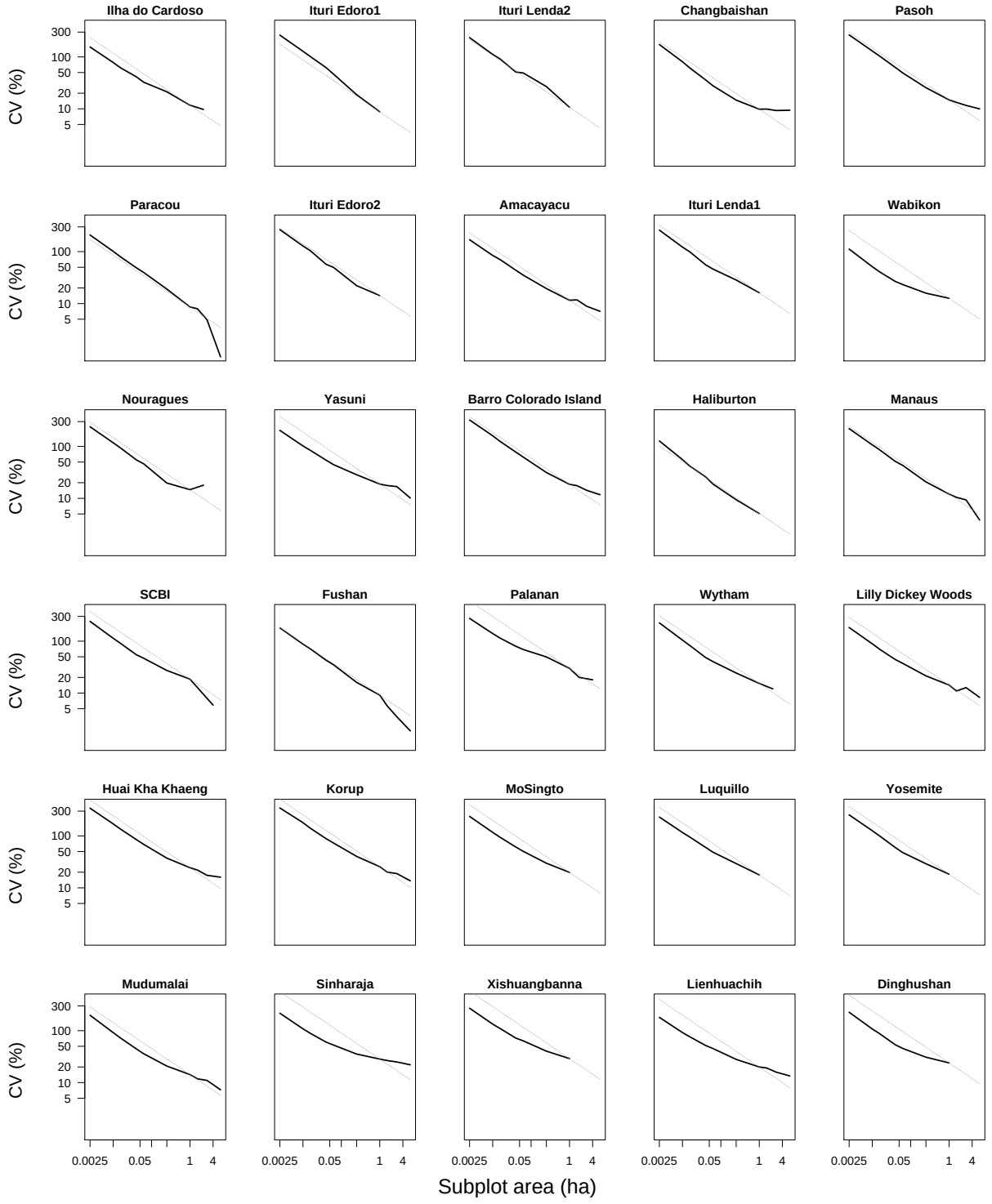

Figure S4. Spatial scaling of the sampling error in *AGB* at each site. The coefficient of variation (CV) of *AGB* is plotted against subplot area, with both on log scales. The grey dotted lines represent the fitted theoretical lines expected if no spatial autocorrelation occurs and CVs at any scale can be predicted from $CV(1)$, the observed CV at 1-ha scales, as $CV(s) = CV(1) \times s^{-\frac{1}{2}}$. Panels are ordered by elevation range.

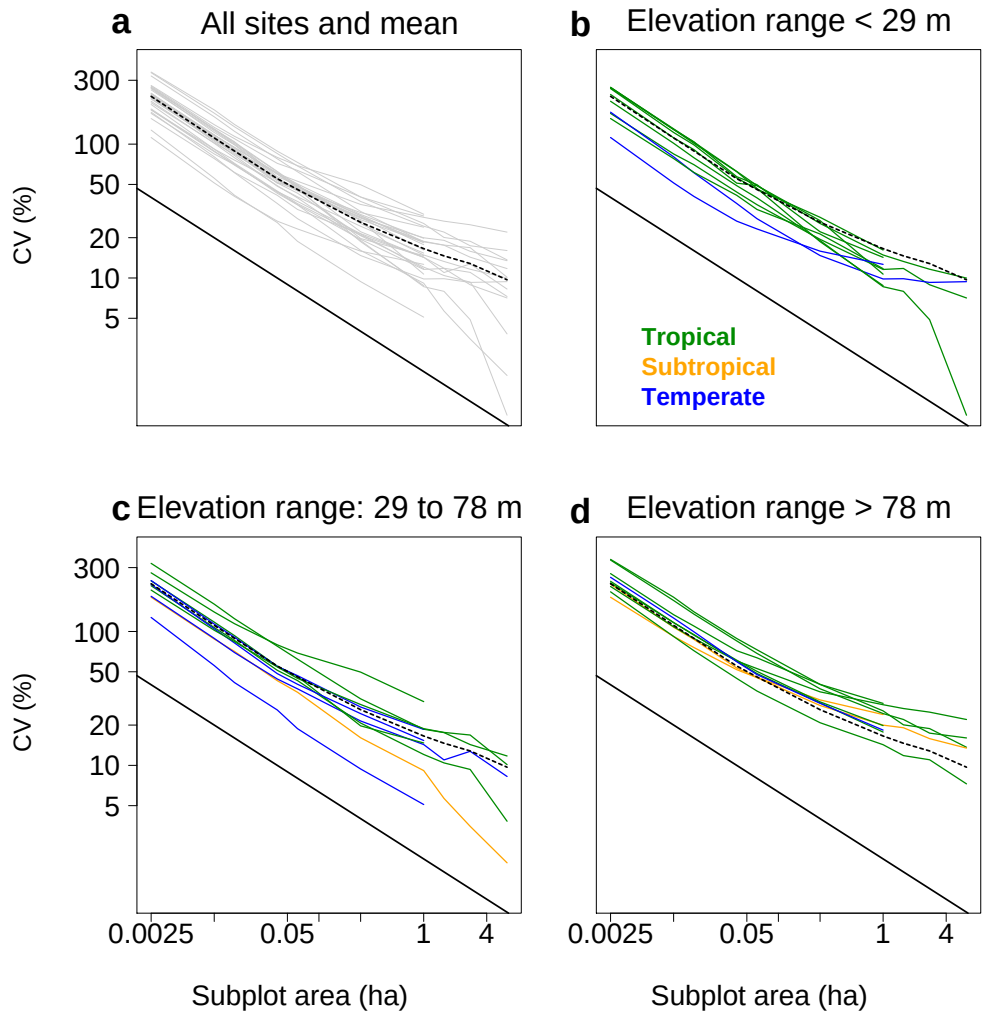

Figure S5. Spatial scaling of sampling error in *AGB* within sites varying in topographic heterogeneity (panels) and forest types (line colors). The coefficient of variation (CV) of *AGB* is plotted against subplot area for each site, with both on log scales. The dotted black line shows the mean CV over all sites (to facilitate comparison across panels) and the solid black line shows the slope of -0.5 expected in the absence of spatial autocorrelation in *AGB*. Panel a shows the CV of all sites in grey. Sites with the least topographic relief (b, lowest tercile in elevation range) had on average lower CV of *AGB* than sites with higher topographic relief (c and d show the next terciles). Elevation range of each tercile is given within panels b, c and d. Graphs for each individual site are provided in Figure S3.

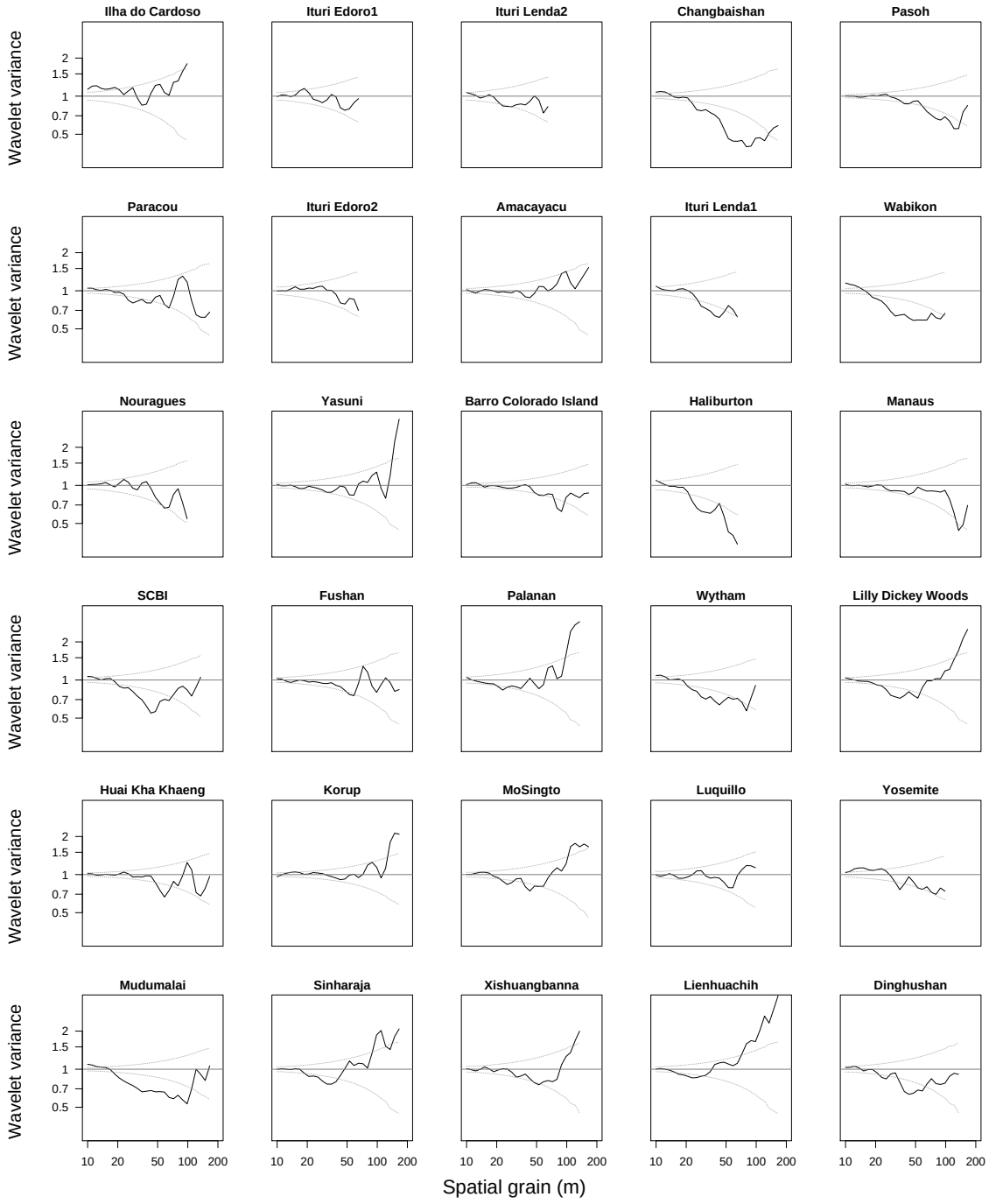

Figure S6. Scale-dependent patterns of spatial autocorrelation, as reflected in the wavelet variance as a function of spatial grain (log scale), for each site (solid black lines). Under no spatial correlation, the wavelet variance is expected to equal 1 (solid grey line). A higher wavelet variance indicates aggregation or clustering at a specific spatial grain, while a lower variance indicates dis-aggregation. The grey dotted lines show the 95% confidence intervals on the null hypothesis of no spatial autocorrelation, as computed from a chi-square distribution with *k* degrees of freedom, where *k* depends on the total area and the considered spatial grain. Panels are ordered by elevation range.

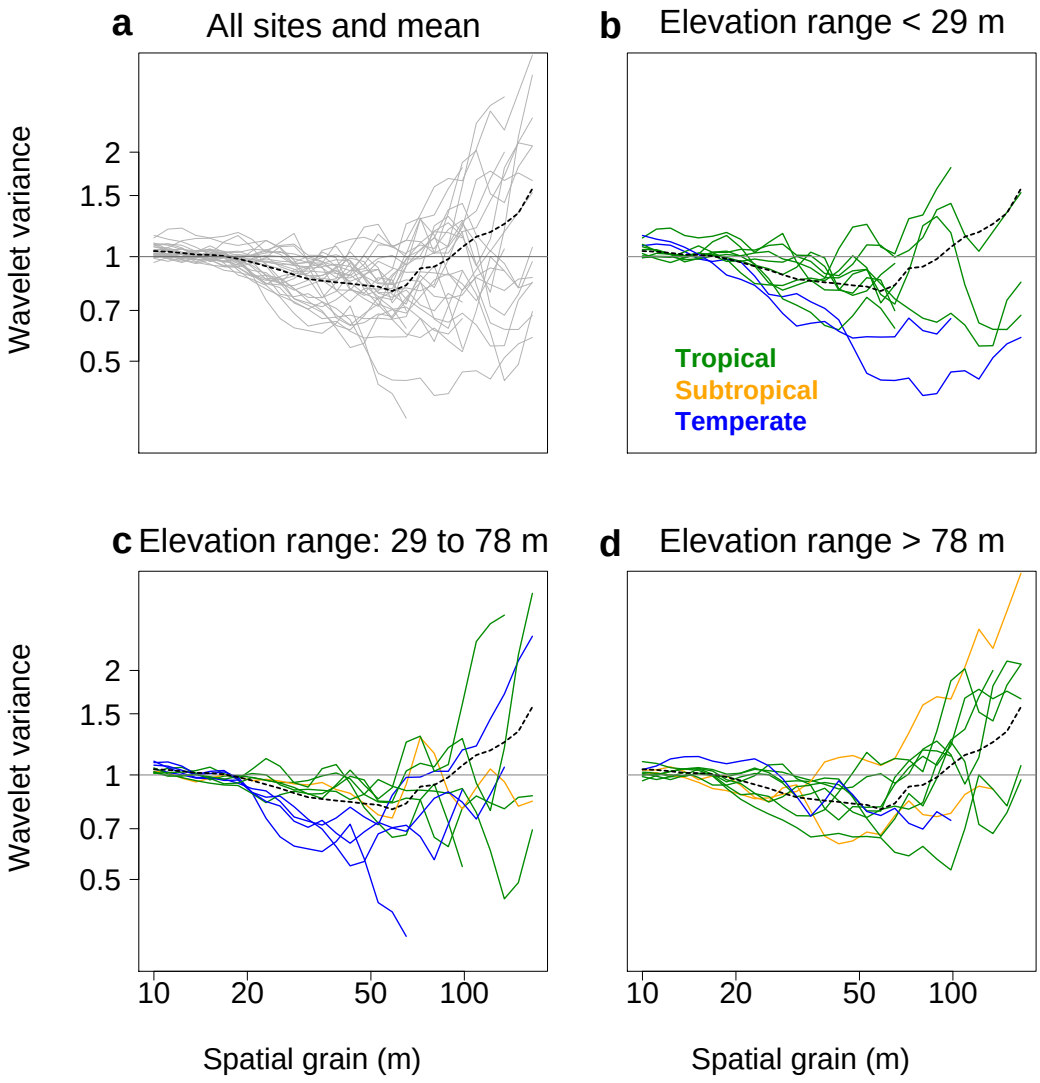

Figure S7. Scale-dependent patterns of spatial autocorrelation within sites varying in topographic relief (panels) and forest types (line colors), as reflected in the wavelet variance as a function of spatial grain. In the absence of spatial autocorrelation, the wavelet variance is expected to equal 1 irrespective of spatial grain (solid grey line). A higher wavelet variance indicates aggregation or clustering at a specific spatial grain, while a lower variance indicates dis-aggregation. The dotted black line shows the ensemble average across all sites to facilitate comparison across panels. Panel a shows the wavelet variance of all sites in light grey. Sites with a greater range of elevation (d) tended to show significant positive spatial autocorrelation at spatial grains of ~100 m and above. Graphs for each individual site, with confidence intervals for the null hypothesis of no spatial correlation, are provided in Figure S5.

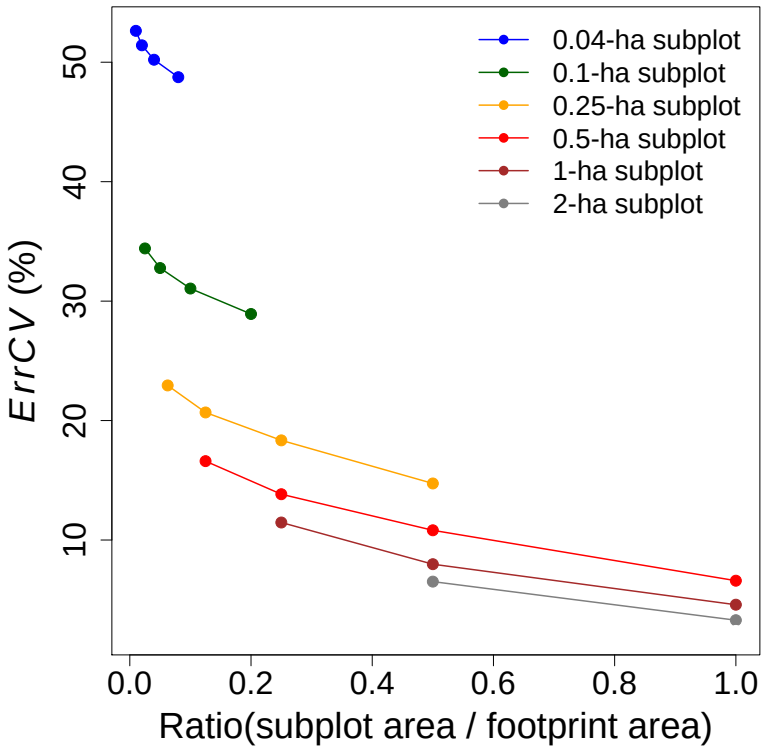

Figure S8. The mean error coefficient of variation (*ErrCV*) in *AGB* as a function of the ratio of the subplot area to the remote sensing resolution for different subplot areas (see key). This figure is based on the simulation scheme described in figure 4.

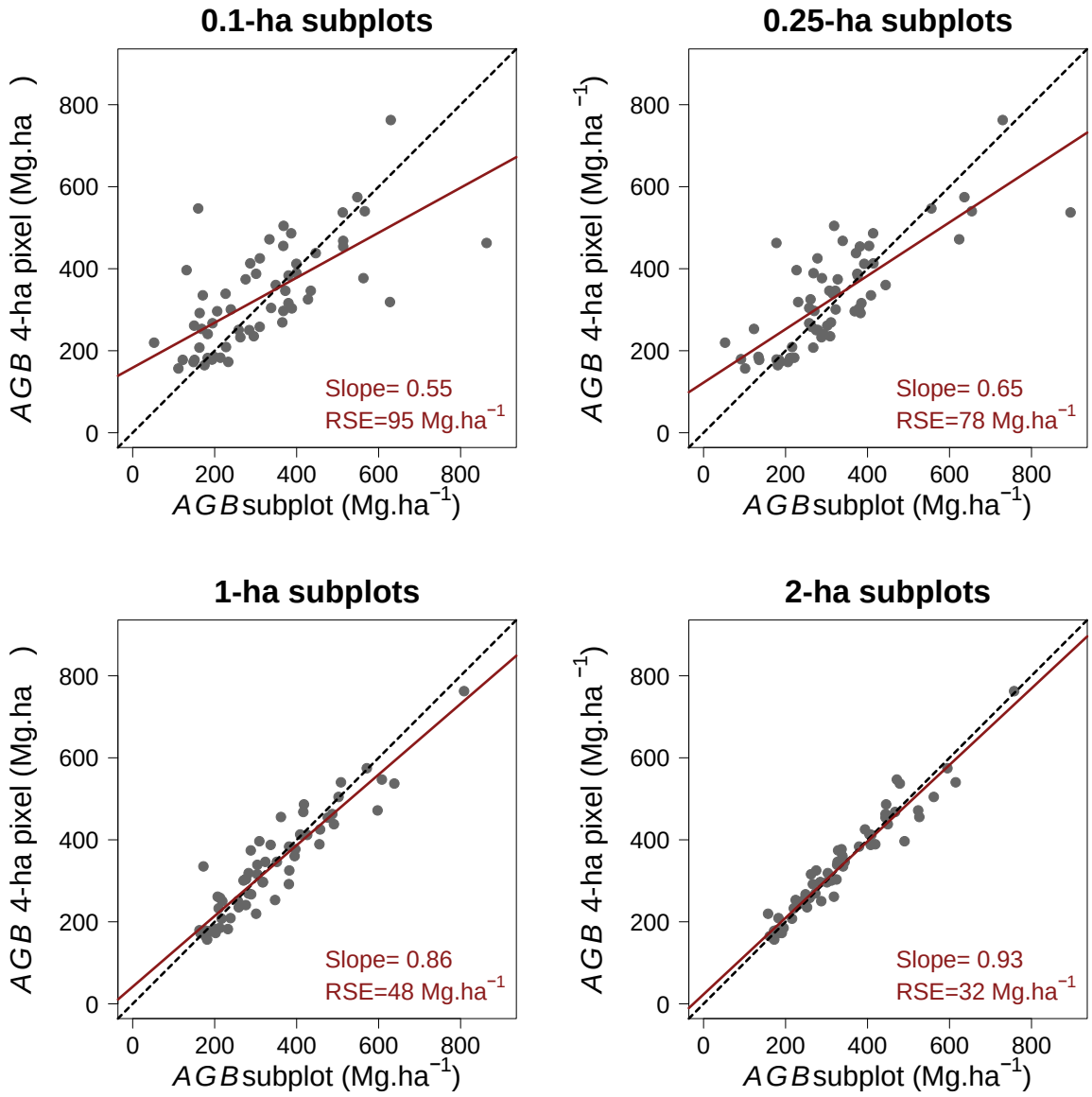

Figure S9. Propagation of field sampling errors to remote sensing products: an example randomly drawn from the 1,000 simulations. Panels illustrate the *AGB* estimated within two 4-ha pixels randomly established in each large plot (n=60, dependent variable) and variable-size subplots located within the 4-ha pixels (independent variable). The regression line obtained from an OLS linear regression between the two *AGB* estimates is shown on each figure (red line). The slope and the residual standard error (RSE) of the model are given in the key. The true slope is one (black dotted line).

TABLES

Table S1. Study site characteristics.

Site	Country	Continent	Lat	Long	Plotdim (m)	Area (ha)	Forest type	Elevation range (m)	Minimum dbh (cm)	Census year	*WSG* values[§]	Allometry used[§]	Mean *AGB* ($Mg.ha^{-1}$)
Amacayacu	Colombia	America	-3.80917	-70.2679	500x500	25	Tropical	22	1	2011	1	2	203.0
Barro Colorado Island	Panama	America	9.1543	-79.8461	1000x500	50	Tropical	40	1	2010	1	2	302.7
Changbaishan	China (Jilin)	Asia	42.3833	128.083	500x500	25	Temperate	17.7	1	2009	-	3	276.9
Dinghushan	China (Guangdong)	Asia	23.1695	112.511	400x500	20	Subtropical	240	1	2005	1	2	249.6
Fushan	Taiwan	Asia	24.7614	121.555	500x500	25	Subtropical	47	1	2009	1	2	175.2
Haliburton	Canada (Ontario)	America	45.2901	-78.6377	400x200*	8	Temperate	50.9	1	2008	-	4	175.5
Huai Kha Khaeng	Thailand	Asia	15.6324	99.217	1000x500	50	Tropical	89	1	2009	1	2	399.1
Ilha do Cardoso	Brazil (São Paulo)	America	-25.0955	-47.9573	300x300*	9	Tropical	5	1	2009	1	2	276.7
Ituri Edoro1	Democratic Republic of Congo	Africa	1.4368	28.5826	200x500	10	Tropical	14	1	2007	1	2	436.5
Ituri Edoro2	Democratic Republic of Congo	Africa	1.4368	28.5826	200x500	10	Tropical	21	1	2007	1	2	432.7
Ituri Lenda1	Democratic Republic of Congo	Africa	1.4368	28.5826	200x500	10	Tropical	24	1	2007	1	2	542.1
Ituri Lenda2	Democratic Republic of Congo	Africa	1.4368	28.5826	200x500	10	Tropical	16	1	2007	1	2	555.4
Korup	Cameroon	Africa	5.07389	8.85472	1000x500	50	Tropical	90	1	2009	1	2	361.8
Lienhuachih	Taiwan	Asia	23.9136	120.879	500x500	25	Subtropical	174	1	2007	1	2	188.6
Lilly Dickey Woods	USA (Indiana)	America	39.2361	-86.2204	500x500	25	Temperate	72	1	2012	-	4	267.8
Luquillo	Puerto Rico	America	18.3262	-65.816	300x500*	15	Tropical	95	1	2000	1	2	358.0
Manaus	Brazil (Amazonas)	America	-2.4417	-59.7858	500x500	25	Tropical	40	1	2007	1	2	322.5
Mo Singto	Thailand	Asia	14.4333	101.35	600x500	30	Tropical	90	1	2005	1	2	310.1
Mudumalai	India (Tamil Nadu)	Asia	11.5989	76.5338	1000x500	50	Tropical	140	1	1992	1	2	172.0
Nouragues	French Guiana	America	4.091944	-52.67861	300x400	12	Tropical	29.9	10	2008	1	2	391.5
Palanan	Philippines	Asia	17.0402	122.388	400x400	16	Tropical	55	1	2010	1	2	444.6
Paracou	French Guiana	America	5.25	-52.91667	500x500	25	Tropical	20.3	10	2009	1	2	405.4
Pasoh	Malaysia	Asia	2.982	102.313	1000x500	50	Tropical	20	1	1990	1	2	336.9
SCBI: Smithsonian Conservation Biology Institute	USA (Virginia)	America	38.8916	-78.1457	400x600*	24	Temperate	43	1	2008	-	4	255.0
Sinharaja	Sri Lanka	Asia	6.4023	80.4023	500x500	25	Tropical	151	1	2002	1	2	563.9
Wabikon Lake Forest	USA (Wisconsin)	America	45.5508	-88.7964	300x800*	24	Temperate	25.9	1	2008	-	4	179.9
Wytham woods	UK	Europe	51.7743	-1.3379	300x600	18	Temperate	60	1	2010	-	5	195.5
Xishuangbanna	China (Yunnan)	Asia	21.6117	101.574	400x500	20	Tropical	160	1	2007	1	2	424.7
Yasuni	Ecuador	America	-0.6859	-76.3953	500x500	25	Tropical	30	1	2002	1	2	285.2
Yosemite National Park	USA (California)	America	37.7662	-119.819	800x300*	24	Temperate	137.2	1	2010	-	6	545.8

* Only a subset of the plot of these dimensions was employed in our analyses, some of which required that both plot dimensions be multiples of 100.

§ 1-Chave *et al.* (2009); 2-Chave *et al.* (2005); 3-Wang *et al.* (2006); 4-Jenkins *et al.* (2003); 5-see Fenn *et al.* (2010); 6-Lutz *et al.*. (2012)

Table S2. Coefficient of variation (*CV*) of *AGB* (in %) according to subplot size in each study plot. The mean *CV* across plots is given at the end of the table for each subplot size.

Field plots	5 m x 5 m	10 m x 10 m	12.5 m x 12.5 m	20 m x 20 m	25 m x 25 m	50 m x 50 m	100 m x 100 m	125 m x 125 m	166.7 m x 166.7 m	250 m x 250 m
Amacayacu	169.51	84.44	70.18	43.84	35.28	19.45	11.58	11.78	8.90	7.09
Barro Colorado Island	322.79	160.09	124.57	77.70	62.14	31.40	18.62	17.57	14.30	11.75
Changbaishan	173.17	80.42	61.12	36.03	27.74	14.71	9.83	9.88	9.26	9.39
Dinghushan	226.08	107.61	87.27	53.36	45.42	30.82	23.96	-	-	-
Fushan	180.30	87.81	71.00	42.96	35.16	16.07	9.14	5.66	3.50	1.87
Haliburton	127.33	55.66	41.52	25.93	18.79	9.40	5.10	-	-	-
Huai Kha Khaeng	341.81	170.43	134.84	85.07	68.59	37.33	24.38	22.02	17.41	16.03
Ilha do Cardoso	155.28	78.01	61.45	41.47	32.50	21.30	11.74	-	-	-
Ituri Edoro1	262.68	128.47	101.42	62.22	46.66	18.69	8.77	-	-	-
Ituri Edoro2	265.75	128.64	104.02	57.08	49.75	22.15	14.26	-	-	-
Ituri Lenda1	259.95	122.20	98.72	55.87	46.12	28.41	16.17	-	-	-
Ituri Lenda2	235.01	111.42	90.92	51.11	48.99	26.81	10.68	-	-	-
Korup	345.59	180.31	140.24	88.67	72.99	40.27	25.53	20.08	18.82	13.66
Lienhuachih	180.23	91.86	75.91	51.87	45.19	28.01	19.97	19.11	15.83	13.46
Lilly Dickey Woods	183.16	88.83	69.62	44.20	37.29	21.45	14.30	10.98	12.73	8.26
Luquillo	230.76	116.36	94.81	60.07	48.53	29.29	17.73	-	-	-
Manaus	219.60	107.05	85.76	51.31	42.96	20.71	12.06	10.43	9.32	3.82
MoSingto	237.24	116.74	93.95	61.06	50.37	29.82	19.81	-	-	-
Mudumalai	197.80	91.78	71.85	44.61	35.90	20.83	14.27	11.83	11.01	7.27
Nouragues	238.87	117.52	93.16	55.09	46.15	19.72	14.69	-	-	-
Palanan	274.28	139.79	114.34	79.58	69.03	49.74	29.93	-	-	-
Paracou	209.01	101.47	79.08	48.94	39.66	19.03	8.61	7.95	4.89	0.94
Pasoh	264.98	130.06	103.31	62.52	49.04	25.54	14.85	13.29	11.63	9.98
SCBI	240.22	113.79	90.52	54.86	46.78	27.28	18.56	-	-	-
Sinharaja	216.91	108.54	88.76	60.25	52.82	35.42	28.39	26.58	24.98	22.01
Wabikon	112.08	51.30	40.66	26.59	23.24	15.87	12.63	-	-	-
Wytham	224.59	104.72	82.15	48.47	40.33	24.35	15.34	-	-	-
Xishuangbanna	270.57	133.49	109.81	71.85	63.58	40.28	29.03	-	-	-
Yasuni	203.75	102.22	83.93	54.36	44.61	28.48	18.80	17.61	16.86	10.13
Yosemite	254.02	125.91	99.44	59.47	47.68	29.09	18.33	-	-	-
MEAN	**227.44**	**111.23**	**88.81**	**55.21**	**45.78**	**26.06**	**16.57**	**14.63**	**12.82**	**9.69**

Table S3. Coefficients of the linear regression of the logarithm of the coefficient of variation, CV, in AGB against the logarithm of plot area for each site. In the absence of spatial autocorrelation in *AGB*, $CV(s) = CV(1)/s^{\gamma}$ with γ =½. Positive spatial autocorrelation should yield γ <½; negative spatial autocorrelation γ >½. Slopes that are significantly different from ½ are highlighted in bold; those that are significantly higher with bold italics.

Site	R^2	Intercept	γ	CI γ
Amacayacu	0.997	2.374	**0.45**	0.421-0.479
Barro Colorado Island	0.997	2.837	0.482	0.451-0.513
Changbaishan	0.986	2.102	0.489	0.421-0.557
Dinghushan	0.954	2.951	**0.375**	0.280-0.471
Fushan	0.998	2.153	0.505	0.481-0.528
Haliburton	0.996	1.532	0.539	0.499-0.579
Huai Kha Khaeng	0.992	3.068	**0.447**	0.401-0.493
Ilha do Cardoso	0.993	2.413	**0.423**	0.381-0.464
Ituri Edoro1	0.997	2.195	***0.576***	0.543-0.610
Ituri Edoro2	0.993	2.526	0.502	0.452-0.552
Ituri Lenda1	0.988	2.677	0.461	0.403-0.519
Ituri Lenda2	0.992	2.451	0.497	0.446-0.548
Korup	0.994	3.135	**0.441**	0.401-0.480
Lienhuachih	0.983	2.866	**0.365**	0.310-0.419
Lilly Dickey Woods	0.987	2.519	**0.426**	0.369-0.484
Luquillo	0.993	2.787	**0.428**	0.388-0.468
Manaus	0.998	2.413	0.49	0.462-0.518
Mo Singto	0.988	2.858	**0.415**	0.363-0.467
Mudumalai	0.982	2.483	0.442	0.372-0.511
Nouragues	0.986	2.506	0.485	0.420-0.551
Palanan	0.982	3.336	**0.355**	0.299-0.411
Paracou	1	2.186	***0.529***	0.516-0.541
Pasoh	0.997	2.611	0.487	0.455-0.519
SCBI: Smithsonian Conservation Biology Institute	0.982	2.758	**0.429**	0.362-0.496
Sinharaja	0.958	3.151	**0.338**	0.256-0.419
Wabikon Lake Forest	0.943	2.305	**0.359**	0.258-0.461
Wytham woods	0.983	2.582	0.447	0.381-0.514
Xishuangbanna	0.976	3.215	**0.369**	0.303-0.436
Yasuni	0.986	2.811	**0.396**	0.342-0.451
Yosemite National Park	0.987	2.774	0.442	0.384-0.500

Table S4. Topographic structure of the world ecological zones by continents. Metrics were calculated using maps at 3 arc minutes of resolution (~5.6 km²). The global ecological zoning of the FAO (2001) was used to classify ecological zones. Slope and elevation were estimated from the SRTM 30+ / ETOPO1 Global Relief Model (Amante & Eakins, 2009) and continents were assigned based on the global administrative area (http://www.gadm.org/). All these analyses were conducted with the R statistical software (R Development Core Team, 2012) using freely available global maps provided by the spatial-analyst.net project (http://spatial-analyst.net/).

FAO Ecological zones	Africa				Asia				Europe				North America			
	% of cover	Mean elevation	Mean slope	% of steep slope*	% of cover	Mean elevation	Mean slope	% of steep slope*	% of cover	Mean elevation	Mean slope	% of steep slope*	% of cover	Mean elevation	Mean slope	% of steep slope*
Polar					8.8	197	0.004	19	0.1	224	0.010	65	38.7	946	0.005	20
Boreal coniferous forest					16	218	0.003	8	15.9	253	0.005	23	8.1	416	0.003	13
Boreal mountain system					12.5	731	0.013	72	8.8	640	0.015	73	5.8	945	0.018	81
Boreal tundra woodland					5	310	0.007	36		156	0.005	31	11.4	315	0.004	13
Temperate continental forest					6.6	210	0.005	18	29.3	212	0.005	18	6.2	287	0.004	12
Temperate desert					8.7	677	0.005	23	0.5	93	0.006	34	2.2	1523	0.019	76
Temperate mountain system					8	2596	0.026	85	7.2	1129	0.033	94	6.6	1281	0.026	90
Temperate oceanic forest									20.3	179	0.006	25	0.1	226	0.014	63
Temperate steppe					6.2	453	0.004	18	4.1	96	0.003	3	6.7	699	0.003	8
Subtropical desert					2.3	562	0.004	15					2.8	977	0.016	70
Subtropical dry forest	1.3	561	0.018	81	0.2	483	0.026	88	10.8	453	0.018	74	0.2	158	0.011	47
Subtropical humid forest	0.3	469	0.015	86	3.1	429	0.017	69	0.2	238	0.022	72	2.8	89	0.002	2
Subtropical mountain system	1.5	1557	0.017	64	5.6	2574	0.038	96	2.7	1202	0.029	88	1.6	1509	0.027	91
Subtropical steppe	1.7	620	0.009	43	1.9	883	0.017	67	0.1	313	0.056	99	3	942	0.008	33
Tropical desert	30.6	449	0.004	14	4	470	0.006	22								
Tropical dry forest	12.1	644	0.005	23	2.1	248	0.006	26					0.5	543	0.023	81
Tropical moist deciduous forest	15.1	737	0.006	26	2	318	0.014	53					1.6	301	0.016	46
Tropical mountain system	4.8	1549	0.025	87	1.2	1411	0.045	98					0.6	1729	0.043	97
Tropical rainforest	12.8	484	0.005	22	4.1	256	0.018	57					1	415	0.027	75
Tropical shrubland	19.7	611	0.005	18	1.7	353	0.005	18					0.1	376	0.040	100

* percentage of area with a slope superior to the 75 percentile of all the slope observed in the world's land area (≥0.068° at 3 arc-min resolution)

Table S4 (continued).

Oceania				South America			
% of cover	Mean elevation	Mean slope	% of steep slope*	% of cover	Mean elevation	Mean slope	% of steep slope*
2.6	848	0.024	89	0.6	1084	0.037	98
3	348	0.018	73	1.9	417	0.026	87
				3.8	544	0.011	55
48.5	304	0.002	3				
1.6	181	0.005	21	0.7	538	0.022	73
3.5	304	0.013	70	7.5	252	0.004	18
				1.5	2751	0.053	100
18	226	0.003	11	4.2	566	0.010	35
				0.8	788	0.027	89
5	136	0.005	22	9.3	357	0.007	29
0.3	53	0.004	13	23.6	351	0.006	26
0.8	2086	0.062	100	10.3	2627	0.045	93
5	347	0.029	71	35.3	200	0.005	14
11.8	232	0.004	13	0.6	570	0.028	72

References cited in supplementary information:

Amante, C. and Eakins, B. W.: ETOPO1 1 Arc-minute global relief model:procedure, data sources and analysis, National Geophysical Data Center. Marine Geology and Geophysics Division, Boulder, Colorado., 2009.

Chave, J., Andalo, C., Brown, S., Cairns, M., Chambers, J., Eamus, D., Fölster, H., Fromard, F., Higuchi, N., Kira, T., Lescure, J.-P., Nelson, B., Ogawa, H., Puig, H., Riéra, B. and Yamakura, T.: Tree allometry and improved estimation of carbon stocks and balance in tropical forests, Oecologia, 145(1), 87–99, doi:10.1007/s00442-005-0100-x, 2005.

Chave, J., Coomes, D., Jansen, S., Lewis, S. L., Swenson, N. G. and Zanne, A. E.: Towards a worldwide wood economics spectrum, Ecology Letters, 12(4), 351–366, 2009.

FAO: Global Ecological Zoning for the Global Forest Resources Assessment 2000, FAO, Rome., 2001.

Fenn, K., Malhi, Y., Morecroft, M., Lloyd, C. and Thomas, M.: Comprehensive description of the carbon cycle of an ancient temperate broadleaved woodland, Biogeosciences Discuss., 7(3), 3735–3763, doi:10.5194/bgd-7-3735-2010, 2010.

Jenkins J.C., Chojnacky D.C., Heath L.S. and Birdsey R.A.: National-Scale Biomass Estimators for United States Tree Species, Forest Science, 49(1), 12–35, 2003.

Lutz, J. A., Larson, A. J., Swanson, M. E. and Freund, J. A.: Ecological Importance of Large-Diameter Trees in a Temperate Mixed-Conifer Forest, PLoS ONE, 7(5), e36131, doi:10.1371/journal.pone.0036131, 2012.

R Development Core Team: R: A language and environment for statistical computing., Vienna, Austria., 2012.

Wang, C.: Biomass allometric equations for 10 co-occurring tree species in Chinese temperate forests, Forest Ecology and Management, 222(1–3), 9–16, doi:10.1016/j.foreco.2005.10.074, 2006.